
Slot-BERT: Self-supervised Object Discovery in Surgical Video

Guiqiu Liao¹ Matjaz Jogan¹ Marcel Hussing² Kenta Nakahashi³ Kazuhiro Yasufuku³ Amin Madani⁴
Eric Eaton² Daniel A. Hashimoto^{1,2}

Abstract

Object-centric slot attention is a powerful framework for unsupervised learning of structured and explainable representations that can support reasoning about objects and actions, including in surgical video. While conventional object-centric methods for videos leverage recurrent processing to achieve efficiency, they often struggle with maintaining long-range temporal coherence required for long videos in surgical applications. On the other hand, fully parallel processing of entire videos enhances temporal consistency but introduces significant computational overhead, making it impractical for implementation on hardware in medical facilities. We present Slot-BERT, a bidirectional long-range model that learns object-centric representations in a latent space while ensuring robust temporal coherence. Slot-BERT scales object discovery seamlessly to long videos of unconstrained lengths. A novel slot contrastive loss further reduces redundancy and improves the representation disentanglement by enhancing slot orthogonality. We evaluate Slot-BERT on real-world surgical video datasets from abdominal, cholecystectomy, and thoracic procedures. Our method surpasses state-of-the-art object-centric approaches under unsupervised training achieving superior performance across diverse domains. We also demonstrate efficient zero-shot domain adaptation to data from diverse surgical specialties and databases. Code and data shared at: <https://github.com/PCASOlab/slot-BERT>.

1. Introduction

Research suggests that humans learn to perceive the world through object-specific grouping and association (Kahne-man et al., 1992; Tenenbaum et al., 2011). This ability constructs representations akin to object files that bind and track features of an object over time thereby enabling more efficient use by downstream cognitive tasks. Inspired by this cognitive process, self-supervised object-centric learning aims to learn explainable and adaptable representations from unlabeled datasets (Burgess et al., 2019; Greff et al., 2019; Locatello et al., 2020; Greff et al., 2020).

While object-centric learning comes in different forms, one particularly effective approach incorporates the inductive bias of grouping or binding low-level, unstructured perceptual activations into a set of vectors known as slots. Each slot encapsulates a higher-level compositional entity, such as an object. This grouping or binding process emerges from architectural priors combined with self-supervised learning techniques, including attention and auto-encoding through specialized encoder-decoder architectures. Substantial progress has been made in this field for both image (Seitzer et al., 2023; Fan et al., 2024; Mansouri et al., 2023; Jiang et al., 2023; Wu et al., 2023b) and video (Weis et al., 2020; Kipf et al., 2022; Aydemir et al., 2023; Zadaianchuk et al., 2023; Wu et al., 2023a; Biza et al., 2023; Lee et al., 2024; Qian et al., 2023; Bao et al., 2022b; 2023; Singh et al., 2022; 2024) processing.

In object-centric image processing, features like color and semantic embeddings from pre-trained models are used to learn pixel-to-object assignments. Methods proposed for object-centric processing of video add additional cues about the temporal consistency of objects, including optical flow (Kipf et al., 2022) and between-frame similarities (Zadaianchuk et al., 2023) or depth maps (Elsayed et al., 2022). While beneficial, these additional cues can lead to increased computational complexity and a higher risk of error accumulation. For instance, optical flow often fails with static or deformable objects and large inter-frame displacements, while depth maps may be not available for certain video domains and unreliable in low-light or low-contrast settings. Feature similarity can address certain challenges but may result in homogeneity when training on smaller datasets

¹Penn Computer Assisted Surgery and Outcomes Laboratory, Department of Surgery, University of Pennsylvania, Philadelphia, PA, USA. ²Department of Computer and Information Science, University of Pennsylvania, Philadelphia, PA, USA. ³Division of Thoracic Surgery, Toronto General Hospital, University Health Network, Toronto, Ontario, Canada. ⁴Surgical Artificial Intelligence Research Academy, University Health Network, Toronto, ON, Canada. Correspondence to: Guiqiu Liao <guiqiu.liao@pennmedicine.upenn.edu>.

as the similarity map is agnostic to the semantics of these features.

These issues become especially pronounced in learning disentangled representation for scene decomposition in surgical videos, where temporal dynamics can be highly complex. Instruments and tissues in surgical videos often move at different speeds, and the visibility of specific objects can fluctuate significantly over the course of a procedure. Moreover, many current object-centric learning approaches for videos fail to fully exploit the sequential structure of longer episodes. In surgical videos, a typical episode depicting a surgical action or a surgical task will last from a few seconds to a minute or longer. (Kipf et al., 2022; Singh et al., 2022; Elsayed et al., 2022) struggle with learning from sequences of this length. Employing slot-attention mechanisms to process entire video sequences in parallel, as proposed in (Singh et al., 2024), could help overcome some challenges but may struggle with scalability for longer videos in real-world datasets due to computational limitations.

These limitations underscore the need for an architecture that is computationally tractable for longer video sequences and supports self-supervised training without auxiliary cues which are not inherently robust (e.g., optical flow or between-frame patch similarity). An ideal model would operate in the latent space that supports scalable temporal reasoning well beyond the short effective context of autoregressive RNNs.

We propose an architecture that is both easy to train and excels in long-range bidirectional temporal reasoning to efficiently handle longer video sequences — Slot-BERT, an self-supervised object-centric slot attention model that performs temporal reasoning over slots using a bidirectional transformer encoder. The model treats slots learned from video frames as foundational visual concepts, similar to how text embeddings represent words. By adapting the BERT transformer encoder from natural language processing to process encoded video slots (akin to a sequence of word embeddings), Slot-BERT learns to reconstruct video feature maps, providing implicit supervision for object discovery through masked auto-encoding of slots. This approach implements a temporal bidirectional self-attention mechanism, enabling effective video representation learning. Furthermore, by learning to reconstruct masked slots, Slot-BERT can predict future slots, and we can use this functionality for future initialization of slots that improves the accuracy when applied on longer sequences. We also propose a video slot contrastive loss that increases the independence between slots within a video by maximizing orthogonality in the latent vector space. This regularization leads to a more distinct representation of concepts and increases the precision of segmentation maps.

To summarize, our contributions are as follows:

- We introduce Slot-BERT, a novel object-centric self-supervised representation learning model based on bidirectional temporal reasoning across video frames.
- We introduce slot-contrastive loss, specifically designed for slot attention, to improve orthogonality between slots.
- Our model is computational efficient and easy to train on longer videos, and can run on affordable hardware.
- We demonstrate superior temporal coherence, bidirectional reasoning, and zero-shot generalization compared to state-of-the-art methods across four surgical video datasets from three different domains.

2. Related Work

2.1. Self-supervised object-centric learning

Learning of object-centric representations can demonstrably improve the sample efficiency and generalization of vision and dynamics models in compositional domains. In order to discover objects from images or videos without supervision, the learning architecture must bind the distinct features that belong to particular objects and create representations with activation patterns that are distinct for object instances. Various approaches have been proposed to achieve this goal. Early works focused on variational auto-encoders (VAEs) (Kingma & Welling, 2014) and disentangled representation learning (Mathieu et al., 2019; Eastwood & Williams, 2018; Kim & Mnih, 2018; Higgins et al., 2017). Other efforts employed iterative attention mechanisms, such as Capsule Networks (Sabour et al., 2017; Hinton et al., 2018; Tsai et al., 2020), contrastive learning approaches (Kipf et al., 2020; Hénaff et al., 2022; Xu et al., 2022), or complex-valued auto-encoders that implicitly encode temporal correlation (Löwe et al., 2022). Beyond learning generalized representations, reconstructive and generative object-centric models also show the ability to segment objects in scenes (Lin et al., 2020; Van Steenkiste et al., 2020; Greff et al., 2019; Engelcke et al., 2020; Burgess et al., 2019).

Slot Attention (SA) (Locatello et al., 2020; Kori et al., 2024), a recently proposed iterative attention mechanism, proved effective in grouping latent representations of objects into a number of slots, and can scale to real-world scenes by reconstructing pre-trained features from foundation models like DINO (Caron et al., 2021) or MAE (He et al., 2022). SA can use multiple modalities to discover objects, such as optical flow (Kipf et al., 2022), depth maps (Elsayed et al., 2022), temporal feature similarity (Zadaianchuk et al., 2023), or 3D point clouds (Ibrahim et al., 2023). Furthermore, SA can embed object entities in an identifiable manner (Kori et al., 2024), with promising results demonstrated on synthetic data. It has also been applied to improve Vision-Language

Modeling (Xu et al., 2024) and controllable synthetic image generation (Jiang et al., 2023; Wu et al., 2023b).

In video processing, association of slots across time requires initialization and SA on video typically uses RNN-like architectures (Kipf et al., 2022; Zadaianchuk et al., 2023; Singh et al., 2022; Elsayed et al., 2022) that support iterative initialization of slots. These approaches however suffer from instability when training on longer sequences and in scenes with a limited temporal coherence. A parallelized approach, such as (Singh et al., 2024), processes the entire video sequence as a batch, which comes at the cost of computational efficiency and makes it less suitable for real-world video applications.

Our SA architecture builds on the RNN framework by incorporating a temporal fusion transformer to enhance long-range bidirectional reasoning, which is inspired by BERT for language modeling (Devlin et al., 2019). We treat the slot representation as a language token and adopt the same pre-training strategy that is used in training of language models to the training of video SA models. This novel design improves temporal coherence and maintains scalability for longer video sequences while addressing the limitations of prior methods.

2.2. Masked Information Encoding

Masked visual modeling has been proposed to learn effective visual representations, starting with training of denoising auto-encoders where masks were treated as noise (Vincent et al., 2010). Transformer architectures (Vaswani et al., 2017) brought significant progress in Natural Language Processing (NLP) (Devlin et al., 2019; Radford, 2018) and vision (Dosovitskiy et al., 2021; Arnab et al., 2021) thanks to learned dot product attention for long-range encoding of co-occurrences. Building upon the success of masked self-attention in GPT (Radford, 2018), iGPT learned to predict sequences of pixels (Chen et al., 2020a) or masked tokens as in the ViT model (Dosovitskiy et al., 2021)

The success of these vision transformers inspired a number of other transformer-based architectures for masked visual modeling (Bao et al., 2022a; Dong et al., 2023; Wei et al., 2022). BEiT (Bao et al., 2022a) and BEVT (Wang et al., 2022) followed the language model BERT (Devlin et al., 2019) learning visual representations from images and videos by predicting discrete tokens (Ramesh et al., 2021). Image MAE (He et al., 2022) and Video MAE (Tong et al., 2022) used asymmetric encoder-decoder architectures for masked image modeling based on plain ViT backbones. MaskFeat (Wei et al., 2022) proposed reconstructing HOG features of masked tokens to perform self-supervised pre-training in videos.

Masked-out features or tokens have also been applied to

weakly supervised settings, where class labels were provided while the objective was to produce attention maps for detection and segmentation (Hou et al., 2018; Lee et al., 2019).

Inspired by BERT, our method treats slots encoded from images as analogous to word embeddings, incorporating a transformer to process video slots. The training objective is to recover image features when slots are partially masked out. Following this strategy, the transformer module can perform reasoning across time instead of merely duplicating information from individual slots.

2.3. Unsupervised Object Detection and Segmentation in Video

Unsupervised object detection and segmentation in videos often rely on motion cues to identify objects and regions of interest. Motion-based approaches have been extensively applied to video segmentation (Fragkiadaki et al., 2015; Kossen et al., 2020; Ponimatkin et al., 2023; Liu et al., 2021; Karazija et al., 2022; Choudhury et al., 2022). For example, Fragkiadaki et al. (Fragkiadaki et al., 2015) ranked segment proposals by combining optical flow with static boundary information. Similarly, Tokmakov et al. (Tokmakov et al., 2017) utilized optical flow to capture motion cues; however, their method struggles to segment static objects due to the lack of detailed spatial information.

To address these challenges, MATNet (Zhou et al., 2020) incorporated motion information to enhance spatiotemporal object representation. While this fusion of static and motion data improved performance, it encountered difficulties with complex moving backgrounds and was highly dependent on the accuracy of optical flow maps. In the domain of surgical videos, Sestini et al. (Sestini et al., 2023) employed a teacher-student network to refine optical flow-based segmentation, improving accuracy in these specialized scenarios.

Beyond motion-based methods, Croitoru et al. (Croitoru et al., 2019) proposed using Principal Component Analysis (PCA) to isolate foreground objects in a fully unsupervised manner. For cases where the segmentation of the first frame is available, tracking-based methods (Uziel et al., 2023; Cheng et al., 2023) can effectively propagate segmentation across video frames. To effectively address the issue of moving background and uncertainty of object presence in surgical videos, an approach using feature ranking and knowledge distillation is proposed (Liao et al., 2024), however this approach needs weak supervision using video-level class labels.

Our work focuses on object-centric learning that produces explainable representations and slot-based segmentation masks at the same time. While we leverage motion cues for object discovery through inductive biases, our method can

learn moving and static objects using a unified framework. By relying solely on a feature reconstruction objective it simplifies the training process while maintaining robustness in handling long-range temporal dependencies. This design allows for more accurate segmentation and object discovery across diverse video domains.

3. Methods

3.1. Overview

We base our object-centric representation learning framework (Figure 1) on slot attention with RNN (Kipf et al., 2022; Singh et al., 2022; Elsayed et al., 2022). A video sequence $V \in \mathbb{R}^{W \times H \times C \times T} = \{I_1, \dots, I_t, \dots, I_T\}$, where $I_t \in \mathbb{R}^{W \times H \times C}$ is an image at time step t of size $W \times H$ with C channels, and T is a fixed length of the video clip that our model operates on, is encoded using a self-supervised feature extraction model to obtain $X \in \mathbb{R}^{N \times D_{feature} \times T}$. Following a recurrent iterative attention approach we obtain the slots representation $S_{initial} \in \mathbb{R}^{K \times d_{slot} \times T} = \{s_1, \dots, s_t, \dots, s_T\}$, where $s_t \in \mathbb{R}^{K \times d_{slot}}$ are the latent space slots that embed objectness information of image I_t . A **Temporal Slot Transformer (TST)** module feeds $S_{initial}$ to a masked transformer encoder which allows elements s_t to attend to each other and aggregate the long-distance information to form S_{final} . An image decoder then recurrently maps each element s_t of S_{final} to the video encoding space $X_{recon} \in \mathbb{R}^{N \times D_{feature} \times T}$. The main training objective is to minimize the distance between the reconstructed feature and the original feature representation X .

3.2. Temporal recurrence of object-centric slot encoder

We encode patches of size $P \times P$ from individual input frames using the **Vision Transformer (ViT)** encoder, producing a stack of patch feature embeddings $X \in \mathbb{R}^{N \times D_{feature} \times T}$, where $N = w \times h$ and $(h, w) = (H/P, W/P)$.

Features $x \in \mathbb{R}^{N \times D_{feature}}$ representing one individual image are grouped by the slot attention module f_{SA} (Locatello et al., 2020) into K spatial groupings through iterative competitive attention and encoded into K slots $s \in \mathbb{R}^{K \times d_{slot}}$. Let W_k, W_v denote the key and value transformation matrices acting on x , and W_q the query transformation matrix acting on s . The iterative slot update function is based on dot attention:

$$s^{i+1} := f_{SA}(x, s^i) = \hat{A}v \quad (1)$$

$$\hat{A}_{mn} := \frac{A_{mn}}{\sum_{l=1}^N A_{ml}} \quad (2)$$

$$A := \text{softmax} \left(\frac{qk^T}{\sqrt{d}} \right) \in \mathbb{R}^{K \times N} \quad (3)$$

where $q = W_q s^i \in \mathbb{R}^{K \times d_{slot}}$ is the query vector, $k = W_k x \in \mathbb{R}^{N \times D_{feature}}$ is the key vector, $v = W_v x \in \mathbb{R}^{N \times D_{feature}}$ is the value vector, and $A \in \mathbb{R}^{K \times N}$ is the attention matrix. $\hat{A} \in \mathbb{R}^{K \times N}$ is the normalized attention used for aggregation, $m \in \{1, \dots, K\}$ is the slots index, $n \in \{1, \dots, N\}$ indexes the input features, and $l \in \{1, \dots, N\}$ is the summation index over features.

Slot attention can be seen as a version of self-attention (Vaswani et al., 2017) constrained by an object-centric inductive bias that is much more computationally efficient as the attention query is much smaller ($K \ll N$, e.g. $N = 784$ for patches, $K = 5 \sim 20$ for objects in an image).

The assignment of slots across video frames is initialized by a RNN-like computation where slots $s_t^{i=0} = \hat{s}_{t-1}$ for t -th frame are initialized by the previous frame's final slot estimation. First frame's slots $s_0^{i=0}$ are initialized randomly by sampling from a standard Gaussian. In this way, the permutation of groupings of objects across slots is likely to remain the same at neighboring frames. However, this assignment could not guarantee temporal consistency for longer video sequences. We thus introduce the **TST** module to enhance long-range bidirectional reasoning along the temporal dimension.

3.3. Temporal slot transformer

The **TST** module facilitates interactions across time steps and enables robust temporal consistency by leveraging positional embeddings and masked training. It processes a sequence of slots $S \in \mathbb{R}^{K \times d_{slot} \times T}$, where T is the number of frames, K is the number of slots, and d_{slot} is the slot dimension. The module comprises the following components:

Temporal Positional Embeddings A learnable positional embedding $P_{temporal} \in \mathbb{R}^{1 \times d_{slot} \times T}$ is added to the slots to encode temporal information:

$$S_{pos} = S + P_{temporal}. \quad (4)$$

Masked Transformer Encoder To promote robust learning, and allow **TST** to have bidirectional reasoning ability (i.e., can predict previous and next slots) we employ random masking during training. For a given masking ratio γ , a subset of frames is masked by setting their corresponding slot values to zero:

$$S_{masked} = S_{pos} \odot M_{slot}, \quad M_{slot} \in \{0, 1\}^{1 \times 1 \times T}, \quad (5)$$

where M_{slot} is the binary mask, and \odot represents element-wise multiplication. The masked slots are then processed

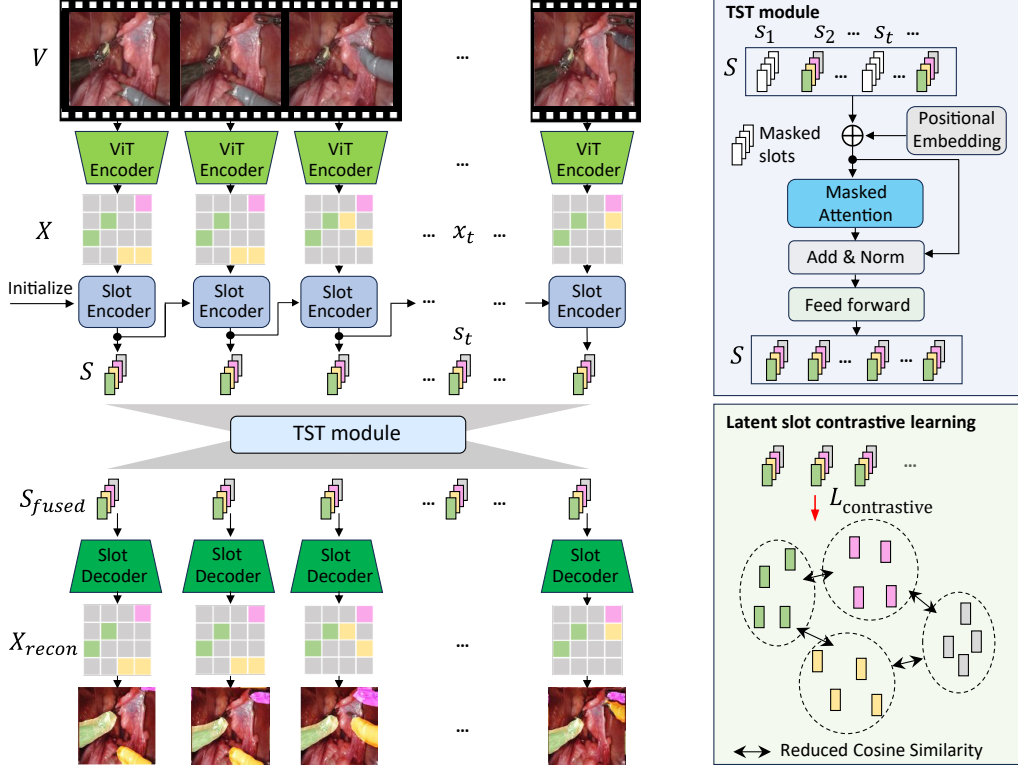


Figure 1. Overview of our object-centric representation learning framework. Video sequences are encoded into features, processed with a recurrent slot attention mechanism, and refined using a Temporal Slot Transformer (TST). The final slot representations are decoded to reconstruct the input features, with training optimized to minimize reconstruction loss and slot contrastive loss.

through a Multi-head Transformer encoder:

$$S_{fused} = \text{TransformerEncoder}(S_{masked}, M_{slot}), \quad (6)$$

Our masked transformer implementation follows previous work in language modeling (Devlin et al., 2019). The key to *bi-directionality* is that the self-attention mechanism is non-causal, in contrast to RNN-like models. Self-attention computes dependencies across all time steps simultaneously, allowing each slot to attend to both past and future frames. During training, the model is tasked with reconstructing the original S_{pos} from S_{masked} , which encourages learning temporally coherent representations that exploit information from the entire sequence in both directions. This design explicitly enables reasoning in both temporal directions.

We use 3 layers of transformer encoder, each with multi-head self-attention ($n_{heads}=8$), feed-forward layers with hidden dimension $4 \times d_{slot}$ and position embedding. The transformer computes attention across all input slots and masked slots M_{slot} , thus modeling dependencies and interactions between unmasked slots effectively. It results in assignments of temporally fused slots $S_{fused} \in \mathbb{R}^{K \times d_{slot} \times T}$. By leveraging temporal positional embeddings and masking, the temporal slot transformer achieves robust temporal

alignment and enhances long-range temporal reasoning. In addition, it can also serve as a future slot prediction module.

3.4. Slot decoder

As our training objective is feature reconstruction of individual frames, we apply the decoder to all slots in S at image level to obtain the reconstructed video features $X_{recon} = \{x_1, x_2, \dots, x_T\}$. We experimented with two types of slot decoders.

MLP broadcast decoder A simple MLP broadcast decoder (Watters et al., 2019) has been used in VAE models and previous slot attention research (Seitzer et al., 2023). Each slot among the K slots is broadcast to match the number of spatial patches resulting in N tokens for each slot. A learnable positional encoding is added to each token. These tokens are then processed independently using a shared MLP to output reconstructed features \hat{x}_k and associated alpha masks α_k indicating the slot’s attentive region. The final reconstruction $x \in \mathbb{R}^{N \times D_{feature}}$ is obtained by a weighted

sum:

$$x = \sum_{k=1}^K \hat{x}_k \odot m_k, \quad m_k = \text{softmax}_k(\alpha_k) \quad (7)$$

where \odot denotes element-wise multiplication. The advantage of this simple design is its efficiency: as the MLP is shared across slots and positions, m_k produced by the decoding is directly deployed as object segmentation masks.

SlotMixer decoder The recently introduced SlotMixer decoder (Sajjadi et al., 2022) for 3D object-centric learning has a constant overhead in the number of slots, as it only decodes once per output, requiring less computation. It employs an attention-based approach and operates in three key steps: slots allocation, mixing, and rendering (Sajjadi et al., 2022). The *allocation* step takes as input the slots $s_t \in \mathbb{R}^{K \times d_{slots}}$ and outputs an embedding vector $f \in \mathbb{R}^{N \times d_{slots}}$ using a cross-attention transformer. The *mixing* step is similar to a single-head attention step, using the embedding f as queries and the slots s_t as keys, to form an attention map $A_{mix} \in \mathbb{R}^{N \times K}$, and the slot mix m is obtained as

$$m = s_t A_{mix}, \quad m \in \mathbb{R}^{N \times d_{slot}}. \quad (8)$$

Finally the *rendering* step uses a MLP with position embedding shared with the allocation step to decode m into $x \in \mathbb{R}^{N \times D_{feature}}$, avoiding the need for a broadcast operation. The learned attention matrix A_{mix} is applied as K channel segmentation masks with resolution $N = w \times h$.

Our experimental results demonstrate that, whether using an MLP broadcast decoder or a Slot-Mixer decoder, our method improves upon the vanilla RNN-based baseline and outperforms other state-of-the-art object-centric methods on the surgical video dataset.

3.5. Slot Contrastive Learning

To encourage diversity among slots and reduce redundancy, one possible approach is to adopt clustering-based metrics such as Normalized Mutual Information for designing the loss function. However, inspired by the SimCLR framework (Chen et al., 2020b), we adopt a contrastive learning loss based on cosine similarity, which is more computationally efficient, directly optimizable during training, and guarantees differentiability. Unlike SimCLR, which computes similarity for positive pairs, our loss enhances dissimilarity between negative pairs (Radford et al., 2021). Unlike conventional methods that use contrastive loss to learn a single global image representation, we apply it to encourage dissimilarity among slot representations that decompose the image and represent objects across video frames. Let $u \in \mathbb{R}^{1 \times d_{slot}}$ represent the one of K slot vectors in s_t for a given frame. For each slot vector u_i , we compute its cosine

similarity with all other slots u_j within the same frame:

$$\text{sim}(u_i, u_j) = \frac{u_i \cdot u_j}{\|s_i\| \|s_j\|}. \quad (9)$$

To exclude self-similarity, the cosine similarity matrix $C \in \mathbb{R}^{K \times K}$ is adjusted by subtracting the identity matrix:

$$C_{ij} = \text{sim}(u_i, u_j) - \delta_{ij}, \quad (10)$$

where δ_{ij} is the Kronecker delta (i.e., $\delta_{ij} = 1$ if $i = j$, and 0 otherwise).

The total contrastive loss for each pair of slot vectors across T frames is then computed as:

$$\mathcal{L}_{\text{contrast}} = \frac{1}{T \cdot K^2} \sum_{t=1}^T \sum_{i=1}^K \sum_{j=1}^K \left[-\log \frac{\exp(-C_{ij}/\tau)}{\sum_{k=1}^K \exp(-C_{ik}/\tau)} \right], \quad (11)$$

where $\tau > 0$ is a temperature parameter. By minimizing this loss the cosine similarity between slots is reduced, which will push the slot vectors to different directions in the representation hyper-space, thus increasing the distance between different slot vectors that now lie on a sphere and point in quasi-orthogonal directions.

3.6. Training loss

The main learning objective is to decode final slots to feature space X_{recon} . Reconstruction loss

$$\mathcal{L}_{\text{recon}} = \|X_{\text{recon}} - X\|_2^2 \quad (12)$$

guides the alignment between the original and reconstructed features.

The final loss function combines the reconstruction loss and the contrastive loss:

$$\mathcal{L}_{\text{final}} = \mathcal{L}_{\text{recon}} + \alpha \mathcal{L}_{\text{contrast}}, \quad (13)$$

where α is a scaling factor to balance the two terms.

The inclusion of the contrastive loss ensures that the slot representations remain diverse, while the reconstruction loss helps align the slots with the input features, guiding effective representation learning.

4. Experiments and Results

4.1. Dataset

We evaluate the performance of **Slot-BERT** on 4 surgical video dataset from 3 types of surgery (Table 1):

MICCAI 2022 SurgToolLoc Challenge Data: This dataset consists of 24,642 30 second video clips at 60 FPS collected from animal, phantom, and simulator-based surgeries (Zia

et al., 2023). It includes a total of 13 instrument types, with up to four instruments in a clip. For simplicity, we refer to this dataset as MICCAI. For our use we downsample clips to 1 FPS.

Cholec80: The Cholec80 dataset (Twinanda et al., 2016) contains 80 cholecystectomy surgery videos downsampled to 1 FPS with presence labels for seven surgical tools in each frame. Following the preprocessing steps of a weakly supervised learning study (Liao et al., 2024), we derived a **Transient Object Presence (TOP)** video subset from Cholec80 resulting in 5,296 clips with 30 frames each, in which objects are not necessarily present in every frame, but can rather transition in or out of the field of view. The test set is based on 100 clips from the CholecSeg8K dataset (Hong et al., 2020), which contains 8,000 frames with instrument and anatomy segmentation from 17 Cholec80 videos. To evaluate long-range object-centric tracking under challenging multi-instrument interaction conditions, we curate a separate test set of 20 unseen cholecystectomy videos, each comprising 30-frame (30 s) sequences. These videos feature frequent instrument interactions, occlusions, and repeated instrument entry and exit events, posing a substantial challenge for maintaining temporal identity consistency.

EndoVis 2017 Robotic Instrument Segmentation Challenge Data: This dataset contains 2,400 annotated frames from videos of abdominal surgery sampled at 1 FPS. We generated 480 video clips by grouping five consecutive frames per clip. The data includes seven instrument types with a maximum of four instruments present in a single clip.

Thoracic Robotic Surgery: This dataset includes data from 40 robot-assisted right upper lobectomies (RULs) for lung malignancy performed at the Toronto General Hospital between 2014 and 2023. A total of 264 annotated clips were selected for this study.

Among these four datasets, only the derivative of *Cholec80*, CholecSeg8k provides both instrument and tissue ground truth masks for evaluation, while other datasets provide only instrument masks.

To demonstrate the benefit of applying our method to broader domains, We also evaluate Slot-BERT on non-surgical datasets, including a natural real-world video dataset YT-VIS (Xu et al., 2019) and a synthetic multi-object tracking data MOVi-E (Greff et al., 2022). Results on these two datasets are concluded in Supplementary material H.

4.2. Metrics

We evaluate our approach based on the quality of the slot masks produced by the decoder using four primary metrics: video foreground ARI (FG-ARI) (Greff et al., 2019), video mean best overlap (mBO) (Pont-Tuset et al., 2016),

Table 1. Data summary. Testing sets are based on frames in annotated clips and the rest of the data is used for training. Except for the Thoracic dataset, all frames in annotated clips have segmentation masks.

Procedure	MICCAI		Cholec		Endovis		Thoracic	
	abdominal	cholecystectomy	abdominal	thoracic	abdominal	thoracic	abdominal	thoracic
Number of clips	24642	6300	480	264	480	264	480	264
Frames per clip	30	30	5	30	5	30	5	30
Annotated clips	100	100	480	264	480	264	480	264
Annotated frames	3000	3000	2400	550	2400	550	2400	550
Clips in training set	24542	5296	—	—	—	—	—	—

mean best Hausdorff Distance (mBHD) and CorLoc (Bilen & Vedaldi, 2016) for evaluating localization accuracy. FG-ARI, adapted from a widely-used metric in object-centric research, measures the similarity between predicted object masks and ground truth masks, focusing on how effectively objects are segmented. mBO, on the other hand, evaluates the alignment between predicted and ground truth masks using the intersection-over-union (IoU) metric. For mBO, each ground truth mask is matched to the predicted mask with the highest IoU via Hungarian matching, and the average IoU is computed across all matched pairs. While FG-ARI primarily measures segmentation quality, mBO provides a more comprehensive assessment by including background pixels. Furthermore, the video version of mBO (mBO-V) also accounts for the temporal consistency of masks throughout the video. To explicitly evaluate long-range temporal consistency, we additionally report identity-aware tracking metrics, including the slot-level IDF1 score (Ristani et al., 2016) and Temporal Identity Persistence (T-IDP) (Milan et al., 2016). IDF1 measures identity precision and recall across frames, while T-IDP quantifies the fraction of frames in which each ground-truth instance is consistently associated with the same predicted slot. To facilitate comparisons at the frame level, we include the image-based version of mBO (mBO-F), which is computed on individual frames. This metric evaluates segmentation quality at the image level without considering temporal consistency. Additionally, to assess the boundary accuracy of the predicted masks, we calculate the mean best Hausdorff Distance (mBHD) for the best-overlapping masks produced by the object-centric learning model. CorLoc is also calculated based on overlapped object instance bounding box, given a threshold $\text{IoU} > 0.5$.

4.3. Baseline models

We compare our method with state-of-the-art object-centric algorithms, including SAVi (Kipf et al., 2022), STEVE (Singh et al., 2022), DINOSaur (Seitzer et al., 2023), VideoSaur (Zadaianchuk et al., 2023), and Slot-Diffusion (Wu et al., 2023b).

SAVi (Kipf et al., 2022) is a weakly supervised, recurrent video object-centric method that leverages the temporal dynamics of video data through optical flow. It conditions

the initial slots on the central coordinates of objects. Since our training data lacks any form of supervision, we adopt a fully unsupervised version of SAVi that excludes initial state conditioning.¹

STEVE (Singh et al., 2022) is an unsupervised model designed for object-centric learning in videos. Like SAVi, it employs an RNN-like slot initialization mechanism. However, STEVE replaces the broadcast decoder used in video slot attention with a specialized transformer-based slot decoder conditioned on slots. Its learning objective focuses on reconstructing individual video frames.²

DINOSaur (Seitzer et al., 2023) bridges the slot attention algorithm to real-world images by replacing the traditional image reconstruction objective with feature reconstruction. It can be implemented with feature encoders such as DINO, MAE, MoCo-v3 (Chen et al., 2021), or MSN (Assran et al., 2022), and the encoder can be either Convolutional Neural Networks (CNNs) or Vision Transformers (ViTs). For our comparisons, we use the version based on the DINO ViT feature extractor.³

Video-Saur (Zadaianchuk et al., 2023), is a recurrent video object-centric method that replaces feature map reconstruction with next-frame feature cosine similarity as its reconstruction objective. It also employs a video-specific slot-mixer decoder for object-centric learning. Following the official implementation of Video-Saur, we report results using a combination of feature reconstruction and similarity reconstruction, with the DINO ViT as the feature extractor.⁴

Slot-Diffusion (Wu et al., 2023b) is an object-centric Latent Diffusion Model (LDM) designed for both image and video data. It introduces the replace of the decoding module for object-centric learning with slot-conditioned diffusion generation models. Based on the video version of Slot-Diffusion, similar to the learning objective of other diffusion models (Rombach et al., 2022), we trained it to reconstruct images of surgical videos following its encoding and decoding pipeline⁵.

4.4. Experiment setup

All raw images of video from different datasets were first cropped to remove zero pixels and then resized to 224×224 . For evaluating segmentation masks, they are upscaled to the same size for computing evaluation metrics. Our training

¹<https://github.com/google-research/slot-attention-video/>

²<https://github.com/singhgautam/steve>

³<https://github.com/amazon-science/object-centric-learning-framework>

⁴<https://github.com/martius-lab/videosaur>

⁵<https://github.com/Wuziyi616/SlotDiffusion>

and inference are implemented on a workstation with 503 GB ram based NVIDIA RTX 6000 Ada Generation GPUs. Adam optimizer with a learning rate of 1×10^{-4} and a weight decay of 1×10^{-5} was used for training. All models are trained under batch size of 4.

We first trained the models on the MICCAI and Cholec datasets. Training duration was 80 epochs for MICCAI and 100 epochs for Cholec. Performance of these models was then tested on all annotated frames from the MICCAI and Cholec testing sets. Next, we tested performance in an unsupervised transfer learning scenario. We used the MICCAI pre-trained weights as the original model, fine-tuned them on the Cholec training data for 10 epochs and measured performance on the Cholec testing set. To measure how well the learned object-centric representations generalize to novel, unseen databases without additional training we measured zero-shot segmentation performance by using the MICCAI trained models to segment testing sets in the EndoVis, Cholec, and Thoracic datasets.

For testing, videos were processed by the trained model three times to calculate an average score and standard deviation, ensuring that any potential instabilities in the model’s outputs were accounted for (Wu et al., 2023b). Five processing repetitions were used in ablation studies.

For testing sequences longer than the training context window, we adopt an online recurrent inference strategy with a sliding window. In addition, we evaluate a variant of our model that extends temporal reasoning to longer sequences by duplicating the TST module and using it as a *next-slot initializer*.

4.5. Unsupervised segmentation performance

This section presents the performance of models trained from scratch on MICCAI and Cholec data. Table 2 highlights the effectiveness of our approach across multiple evaluation metrics, demonstrating its robustness to various dataset characteristics.

All methods achieve their highest performance on the MICCAI dataset, reflecting the advantages of having a larger collection of data. Our method surpasses all competing methods in every metric: mBO-V (48.90%; +2.60% increase), mBO-F (52.80%; +2.70% increase), mBHD (44.2; -9.7 decrease), FG-ARI (58.20%; 3.10% increase) and Cor-Loc (70.7%; 10.6% increase). These improvements suggest that the model benefits from the dataset’s scale and diversity. Compared to the closest competitor, Video-Saur, our method significantly improves mBO-V, mBHD and CorLoc metrics, indicating better segment boundary and instance accuracy.

The performance on the Cholec dataset is comparatively lower for all models. Nevertheless, our method outper-

Table 2. Unsupervised training from scratch. Bold values indicate the best performance for each dataset.

Datasets	Method	mBO-V (%)	mBO-F (%)	mBHD (\downarrow)	FG-ARI (%)	CorLoc (%)
MICCAI	DINO-Saur(Seitzer et al., 2023)	38.2 \pm 0.9	42.9 \pm 0.5	62.5 \pm 1.3	48.4 \pm 0.7	45.8 \pm 2.2
	SAVi(Kipf et al., 2022)	29.4 \pm 0.2	33.2 \pm 0.1	81.7 \pm 1.0	36.6 \pm 0.2	40.0 \pm 0.5
	STEVE(Singh et al., 2022)	27.9 \pm 0.2	31.5 \pm 0.1	139.9 \pm 0.6	34.3 \pm 0.1	17.0 \pm 0.4
	Slot-Diffusion(Wu et al., 2023b)	37.5 \pm 0.1	42.2 \pm 0.1	70.5 \pm 0.2	46.3 \pm 0.0	42.0 \pm 0.2
	Video-Saur(Zadaianchuk et al., 2023)	46.3 \pm 0.4	50.1 \pm 0.4	53.9 \pm 1.3	55.1 \pm 0.5	60.1 \pm 1.9
	Ours	48.9 \pm 0.2	52.8 \pm 0.3	44.2 \pm 0.6	58.2 \pm 0.2	70.7 \pm 0.8
Cholec	DINO-Saur(Seitzer et al., 2023)	25.7 \pm 1.0	25.5 \pm 0.5	75.9 \pm 0.6	33.9 \pm 0.7	29.1 \pm 0.5
	SAVi(Kipf et al., 2022)	18.9 \pm 0.2	18.1 \pm 0.1	107.0 \pm 0.2	23.7 \pm 0.1	15.3 \pm 0.1
	STEVE(Singh et al., 2022)	19.5 \pm 0.1	18.7 \pm 0.0	108.9 \pm 0.2	24.2 \pm 0.0	19.8 \pm 0.7
	Slot-Diffusion(Wu et al., 2023b)	12.8 \pm 0.0	15.7 \pm 0.0	91.4 \pm 0.3	19.4 \pm 0.0	18.9 \pm 0.2
	Video-Saur(Zadaianchuk et al., 2023)	26.1 \pm 0.3	25.8 \pm 0.2	74.9 \pm 0.3	34.2 \pm 0.2	34.6 \pm 1.9
	Ours	28.8 \pm 0.3	27.8 \pm 0.4	64.8 \pm 0.9	37.0 \pm 0.6	35.3 \pm 2.0
Cholec + Tissue Mask	DINO-Saur(Seitzer et al., 2023)	30.2 \pm 0.1	36.7 \pm 0.5	90.9 \pm 1.0	41.4 \pm 0.6	22.5 \pm 0.2
	SAVi(Kipf et al., 2022)	27.8 \pm 0.0	29.3 \pm 0.0	117.2 \pm 0.1	35.4 \pm 0.1	16.4 \pm 0.0
	STEVE(Singh et al., 2022)	28.5 \pm 0.0	33.6 \pm 0.1	127.7 \pm 0.0	33.0 \pm 0.0	16.5 \pm 0.1
	Slot-Diffusion(Wu et al., 2023b)	29.3 \pm 0.2	34.0 \pm 0.2	99.1 \pm 0.2	35.5 \pm 0.2	23.3 \pm 0.2
	Video-Saur(Zadaianchuk et al., 2023)	30.9 \pm 0.1	33.7 \pm 0.1	90.3 \pm 0.1	43.1 \pm 0.3	24.8 \pm 0.3
	Slot-BERT (Ours)	33.4 \pm 0.5	40.2 \pm 0.3	85.4 \pm 0.8	44.1 \pm 0.5	25.9 \pm 0.3

[†] We report Cholec results on instruments only (Cholec) for easier comparison to MICCAI, and on both instruments and tissue (Cholec + Tissue Masks).

Table 3. Transfer learning performance of Slot-BERT compared to object-centric SOTA methods. Fine-tuning of the model trained on the larger MICCAI dataset leads to better performance in comparison to models trained from scratch on Cholec.

Methods	mBO-V (%)	mBO-F (%)	FG-ARI (%)
DINO-Saur(Seitzer et al., 2023)	26.3 \pm 1.0	26.0 \pm 0.9	34.7 \pm 1.1
SAVi(Kipf et al., 2022)	18.2 \pm 0.1	17.6 \pm 0.0	23.0 \pm 0.1
STEVE(Singh et al., 2022)	17.4 \pm 0.0	16.7 \pm 0.0	22.1 \pm 0.1
Slot-Diffusion(Wu et al., 2023b)	23.4 \pm 0.1	22.9 \pm 0.1	29.8 \pm 0.1
Video-Saur(Zadaianchuk et al., 2023)	28.7 \pm 0.5	28.3 \pm 0.5	37.3 \pm 0.6
Ours	31.4 \pm 0.6	30.1 \pm 0.3	40.0 \pm 0.7

forms all baselines, with notable gains over Video-Saur (e.g., +2.7% in MBO-V, +2.8% in FG-ARI and -10.1 in mBHD on instrument segmentation; +2.7% in MBO-V when evaluated with tissue masks). It is evident that the smaller size of the dataset and less diversity in the data impact performance compared to MICCAI, the latter being almost five times larger than Cholec. An additional challenge in Cholec dataset is the frequent instrument disappearance/reappearance (Liao et al., 2024) and the small size of some objects which pose a challenge because the slot number is fixed. These data characteristics also result in the phenomenon where mBO-F is smaller than mBO-V, unlike in MICCAI data, where most methods achieve a higher mBO-F instead. Figure 2 presents qualitative results of unsupervised segmentation, illustrating our method’s advantage in delineating instruments from tissue and discriminating tissue with different textures compared to STEVE and SAVi.

4.6. Transfer learning performance

We evaluate the transfer learning performance of Slot-BERT by taking the model trained on the MICCAI dataset and fine-

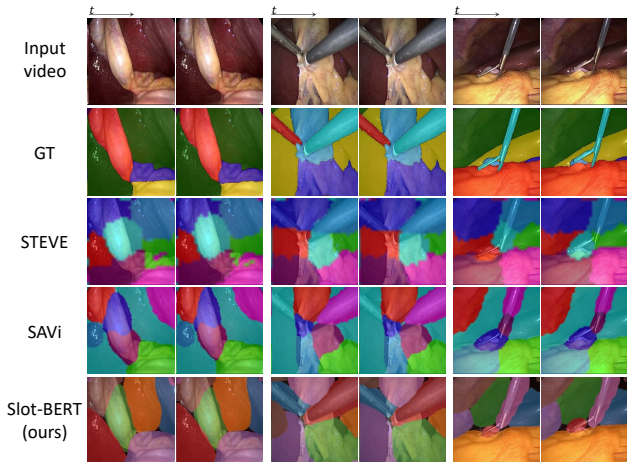


Figure 2. Qualitative results of unsupervised segmentation using STEVE, SAVi and our method on the Cholec dataset, which can be evaluated both tissue and instrument ground truth (GT). Slot-BERT demonstrates a stronger ability to delineate instruments from tissue and to separate tissues with different textures.

tuning it on the Cholec dataset. We fine-tune the model for 10 epochs. Our experiments show that fine-tuning provides significant performance gains over training the model from scratch on the Cholec dataset indicating that object specific representations benefit from training on larger datasets and can be easily reused on smaller datasets.

A comparison of transfer learning performance with SOTA is summarized in Table 3. We observe that Slot-BERT outperforms all other methods in all three metrics, outperforming Video-Saur by 2.7% in mBO-V and FG-ARI.

Fine-tuning results in an increase of 2.6% in *mBO-V*, 2.2% in *mBO-F*, and 3.0% in *FG-ARI* compared to training on Cholec data, confirming the plausibility of transfer learning to leverage large databases and enhance the performance of object-centric models on new datasets.

4.7. Zero-shot performance

Table 4 illustrates the performance of models trained on MICCAI and tested directly on unseen datasets without additional supervision. When comparing the zero-shot results to models trained fully from scratch on the respective testing domains (refer to Table 2), our method demonstrates performance that is highly competitive with domain-specific training, achieving almost identical results on the Cholec database and commendable results on the new EndoVis and Thoracic datasets.

Qualitative results of the zero-shot performance, illustrated in Figure 3, show that our method successfully segments unseen surgical instruments in new surgical scenes. In contrast, methods like STEVE and SAVi exhibit degraded adaptability, failing to capture objectiveness or accurately locate instruments in unseen videos.

As the Thoracic dataset is sparsely annotated (approximately two frames per clip), the *mBO-V* is less relevant than *mBO-F*. Looking at the results for the Thoracic dataset where frame lengths differ significantly compared to Endovis and Cholec, our model still outperforms others, achieving an 2.2% better *mBO-F* and 6.4 decrease in *mBHD* compared to Video-Saur. These results validate the robustness of our model in diverse settings.

Figure 3 also reveals a drawback of our approach for the accuracy of segmentation masks. As the frames are divided into patches, our method is not accurate at detecting precise object boundaries, in particular for instruments, as the immediate background of instruments is highly correlated across scenes. The method tends to however correctly locate the whole object, leading to a low false negative rate.

4.8. Longer and more challenging sequences

To evaluate the robustness and generalization of our method to longer video sequences, we tested our model on sequences of 7 and 11 frames after training on 5 frames. A sliding window approach was employed to handle longer inputs, ensuring temporal alignment during prediction. Additionally, we introduced a future slot prediction mechanism that replaced the simple RNN-based slot initialization which is only possible when testing on video length that is equal to length in training. In this new design, the temporal slot transformer is fed all previous $T - 1$ slots, leaving the slot at the last position empty. The temporal slot transformer then predicts this missing slot, which serves as the initial-

ization for subsequent frames. An illustration of this next slot initialization can be found in supplementary material section B.

The results in Table 5 demonstrate that our method achieves better performance compared to state-of-the-art approaches across all metrics, particularly in terms of *mBO-V*, *mBO-F*, *MBHD* and *FG-ARI*. For instance, in 7-frame sequences, our method achieved an *mBO-V* of 48.0% and an *FG-ARI* of 57.5%, surpassing the next best method, Video-Saur, by 1.3% and 1.4%, respectively. When extended to 11-frame sequences, our method maintained its robust performance, achieving an *mBO-V* of 46.2% and an *FG-ARI* of 56.8%. These results highlight the minimal degradation in accuracy as the sequence length increases, demonstrating the adaptability of our approach.

With the future slot prediction mechanism, we observed further performance gains, particularly for longer sequences with 11 frames. The *mBO-V* increased to 46.9%, and the *FG-ARI* improved to 57.3%, highlighting the effectiveness of this advanced initialization strategy in maintaining temporal coherence.

Figure 4 visualizes the impact of sequence length on accuracy. Across methods, *mBO-F* showed minimal variation with longer sequences, demonstrating that frame-level accuracy is generally stable across sequence lengths. However, the challenge of maintaining temporal consistency is evident in video-level metrics (*mBO-V*). Most methods, including SAVi, STEVE, and Video-Saur, exhibited a notable decline in *mBO-V* with longer sequences. In contrast, our method maintains the highest *mBO-V* among all evaluated methods. This robustness underscores our approach’s ability to adapt to varying temporal contexts effectively.

To further demonstrate performance on even longer temporal context windows, we train and test Slot-BERT on 30 second episodes. The results and comparison to other methods are shown in Table 6. Note that, compared to shorter videos (e.g., 11 frames), the video-level *mBO* score decreased by around 2%. Nevertheless, Slot-BERT beats state-of-the-art approaches across all metrics and maintains a high image-level segmentation accuracy in comparison to training on shorter clips. Note that training on longer sequences is not necessarily beneficial once the temporal structure becomes less informative about frame-to-frame transitions. An optimal training protocol for Slot-BERT would thus take into account the length and complexity of typical surgical actions and tasks.

We evaluate long-range temporal tracking under more challenging conditions, using the additional test set of unseen Cholecystectomy videos, where frequent object occlusions as well as instrument entry and exit occur. This setting reflects realistic surgical workflows and poses a significant

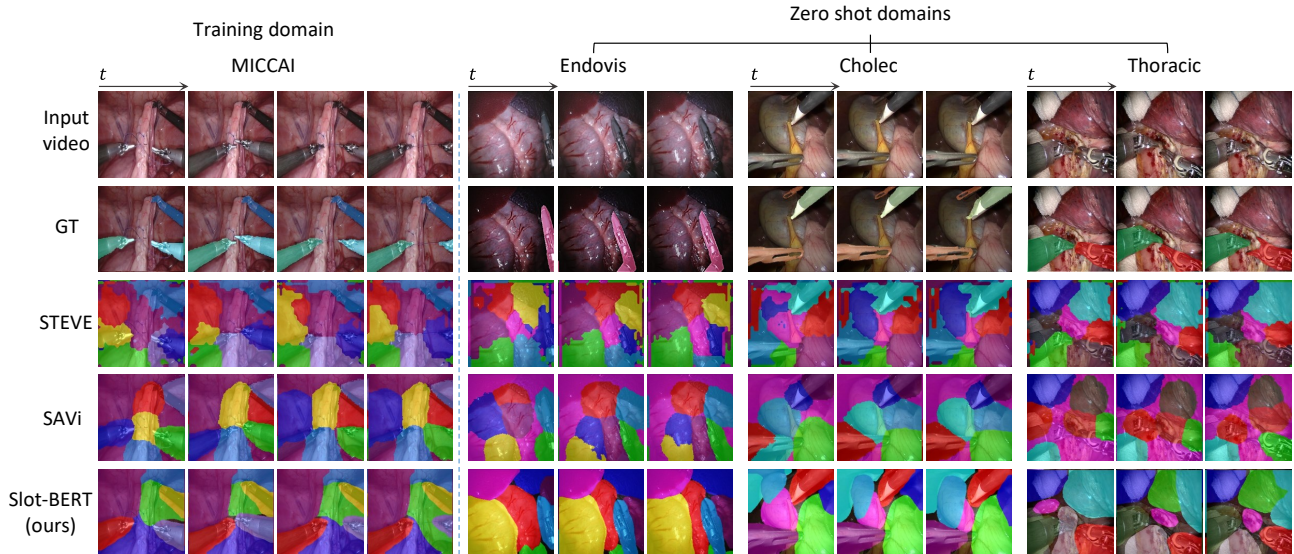


Figure 3. Qualitative results of zero-shot experiments on unseen datasets using our method compared to STEVE and SAVi. Slot-BERT demonstrates superior adaptability, successfully segmenting unseen surgical instruments, while alternative methods exhibit degraded performance. Despite limitations in precise boundary detection due to patch-based processing, our method achieves high object localization coverage.

Table 4. Performance comparison in zero-shot segmentation. Zero-shot results demonstrate the transferability of models pre-trained on MICCAI data when applied to unseen domains. Results with the best mean values are highlighted in bold.

Dataset	Method	mBO-V (%)	mBO-F (%)	mBHD (\downarrow)	FG-ARI (%)
Endovis	DINO-Saur(Seitzer et al., 2023)	34.1 \pm 0.3	38.7 \pm 0.4	64.4 \pm 1.1	45.4 \pm 0.5
	SAVi(Kipf et al., 2022)	28.2 \pm 0.2	32.4 \pm 0.1	81.6 \pm 0.2	36.9 \pm 0.0
	STEVE(Singh et al., 2022)	26.0 \pm 0.1	29.8 \pm 0.1	143.7 \pm 0.2	33.9 \pm 0.1
	Slot-Diffusion(Wu et al., 2023b)	33.3 \pm 0.1	35.9 \pm 0.1	95.6 \pm 0.1	40.6 \pm 0.1
	Video-Saur(Zadaianchuk et al., 2023)	42.7 \pm 0.2	46.7 \pm 0.2	56.2 \pm 0.2	53.5 \pm 0.1
	Ours	43.5 \pm 0.3	47.6 \pm 0.3	50.7 \pm 0.4	54.4 \pm 0.3
Thoracic [†]	DINO-Saur(Seitzer et al., 2023)	27.7 \pm 0.6	34.7 \pm 0.5	90.7 \pm 0.7	28.2 \pm 0.5
	SAVi(Kipf et al., 2022)	24.9 \pm 0.2	28.5 \pm 0.0	105.3 \pm 1.0	21.7 \pm 0.2
	STEVE(Singh et al., 2022)	24.0 \pm 0.0	30.2 \pm 0.1	127.9 \pm 0.6	22.6 \pm 0.0
	Slot-Diffusion(Wu et al., 2023b)	29.3 \pm 0.1	36.9 \pm 0.1	103.1 \pm 0.2	28.1 \pm 0.1
	Video-Saur(Zadaianchuk et al., 2023)	36.7 \pm 0.1	48.9 \pm 0.1	72.8 \pm 0.4	39.2 \pm 0.1
	Ours	37.7 \pm 0.2	51.1 \pm 0.3	66.4 \pm 0.3	40.5 \pm 0.1
Cholec	DINO-Saur(Seitzer et al., 2023)	21.5 \pm 0.8	20.7 \pm 0.4	82.8 \pm 1.3	28.1 \pm 0.9
	SAVi(Kipf et al., 2022)	17.8 \pm 0.1	17.3 \pm 0.1	106.1 \pm 0.7	22.6 \pm 0.1
	STEVE(Singh et al., 2022)	17.3 \pm 0.1	16.6 \pm 0.1	139.2 \pm 0.9	21.9 \pm 0.1
	Slot-Diffusion(Wu et al., 2023b)	17.8 \pm 0.1	17.0 \pm 0.0	106.1 \pm 0.3	20.9 \pm 0.1
	Video-Saur(Zadaianchuk et al., 2023)	27.0 \pm 0.5	26.1 \pm 0.5	72.5 \pm 1.5	35.5 \pm 0.6
	Ours	29.2 \pm 0.1	27.9 \pm 0.1	64.0 \pm 0.6	37.7 \pm 0.0

[†]When zero-shot on thoracic the video length is increased to 30 frames in comparison to Endovis and Cholec (5 frames).

challenge for online object-centric tracking. Long-range tracking performance is assessed using identity-aware metrics, including IDF1 and Temporal Identity Persistence (T-IDP), together with object localization accuracy (CorLoc).

As shown in Fig. 5, we evaluate tracking over sequences of

30 frames and compare our full model against a baseline using vanilla RNN-based inference without TST or contrastive learning. Our real-time method improves average slot-level IDF1 by 9.4%, T-IDP by 8.9%, and CorLoc by 8.8%, demonstrating substantially stronger identity consistency and localization accuracy under frequent object entry

Table 5. Comparison of performance metrics for sequences of 7 and 11 frames. Metrics include mBO-V, mBO-F, mBHD, and FG-ARI. Our method consistently achieves the highest scores across all metrics, with further improvements observed when incorporating the future slot prediction mechanism, showcasing robustness and adaptability to longer sequences. Results with the best mean values are highlighted in bold.

Method	7 Frames				11 Frames			
	mBO-V (%)	mBO-F (%)	mBHD (\downarrow)	FG-ARI (%)	mBO-V (%)	mBO-F (%)	mBHD (\downarrow)	FG-ARI (%)
DINO-Saur(Seitzer et al., 2023)	33.50 \pm 0.90	39.80 \pm 0.20	64.0 \pm 1.9	44.90 \pm 0.30	32.00 \pm 0.30	40.20 \pm 0.40	62.8 \pm 1.1	44.30 \pm 0.40
SAVi(Kipf et al., 2022)	28.80 \pm 0.30	33.50 \pm 0.20	80.9 \pm 0.9	36.90 \pm 0.20	27.40 \pm 0.20	33.70 \pm 0.30	81.7 \pm 0.5	36.00 \pm 0.30
STEVE(Singh et al., 2022)	27.10 \pm 0.10	31.40 \pm 0.10	141.0 \pm 0.7	34.30 \pm 0.10	25.70 \pm 0.00	31.40 \pm 0.00	140.3 \pm 0.7	33.40 \pm 0.00
Slot-Diffusion(Wu et al., 2023b)	35.60 \pm 0.20	38.30 \pm 0.10	79.6 \pm 0.1	41.20 \pm 0.10	34.00 \pm 0.10	38.20 \pm 0.10	80.2 \pm 0.2	40.00 \pm 0.10
Video-Saur(Zadaianchuk et al., 2023)	46.70 \pm 0.30	51.10 \pm 0.20	52.5 \pm 0.9	56.10 \pm 0.30	44.40 \pm 0.30	51.60 \pm 0.20	51.5 \pm 0.4	55.20 \pm 0.20
Ours	48.00 \pm 0.50	52.30 \pm 0.30	44.1 \pm 0.7	57.50 \pm 0.50	46.20 \pm 0.50	53.10 \pm 0.30	43.8 \pm 0.9	56.80 \pm 0.40
Ours + Future slot prediction	48.50 \pm 0.80	52.80 \pm 0.70	44.14 \pm 1.1	58.00 \pm 0.90	46.90 \pm 0.00	53.60 \pm 0.10	43.10 \pm 0.16	57.30 \pm 0.30

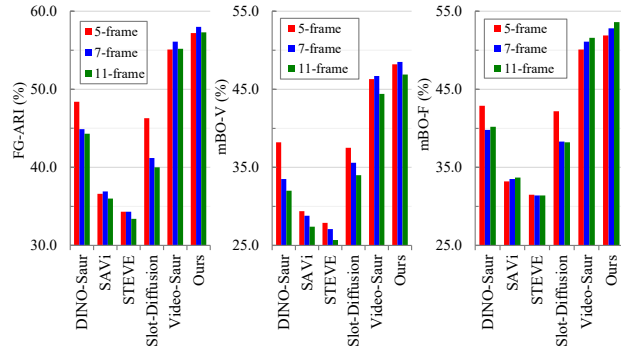


Figure 4. Impact of sequence length on performance. The plot illustrates mBO-F and mBO-V metrics across different sequence lengths for various methods. Our method demonstrates stronger temporal consistency, with minimal degradation in video-level accuracy (mBO-V) as sequence length increases, outperforming SOTA approaches across all evaluated settings.

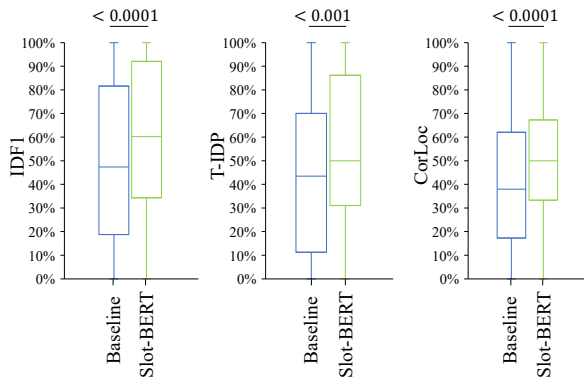


Figure 5. Box plot comparison of Slot-BERT and the baseline in a challenging scenario characterized by frequent object entry and exit. Long-range temporal tracking performance is assessed using IDF1 and Temporal Identity Persistence (T-IDP), together with object localization accuracy (CorLoc).

and exit.

Table 6. Comparison of performance metrics (mBO-V, mBO-F, FG-ARI, and Corloc) video for sequences of 30 seconds. Our method achieves the best results across all metrics, demonstrating robustness and adaptability to long sequences. Results with the best mean values are highlighted in bold.

Method	mBO-V (%)	mBO-F (%)	FG-ARI (%)	Corloc (%)
DINO-Saur(Seitzer et al., 2023)	30.96 \pm 0.29	42.15 \pm 0.09	45.11 \pm 0.41	52.79 \pm 0.71
SAVi(Kipf et al., 2022)	25.39 \pm 0.25	35.23 \pm 0.02	35.98 \pm 0.01	42.56 \pm 0.23
STEVE(Singh et al., 2022)	25.37 \pm 0.06	33.99 \pm 0.01	36.83 \pm 0.01	45.76 \pm 0.06
Slot-Diffusion(Wu et al., 2023b)	30.67 \pm 0.38	40.57 \pm 0.15	43.96 \pm 0.16	52.94 \pm 0.22
Video-Saur(Zadaianchuk et al., 2023)	42.31 \pm 0.09	53.04 \pm 0.07	56.81 \pm 0.32	68.68 \pm 0.39
Slot-BERT (ours)	44.37 \pm 0.27	55.31 \pm 0.09	61.68 \pm 0.25	73.22 \pm 0.24

4.9. Ablation study

We conduct ablation studying by isolating the effects of our two main contributions, namely the slot contrastive objective and the TST module, on video segmentation accuracy and temporal tracking consistency across different datasets and video lengths.

All ablation experiments are repeated across five independent runs, resulting in 500-1000 total video-level evaluations per experiment. Statistical significance is assessed using one-tailed Welch’s t -tests and Bonferroni correction for multiple comparisons. The observed improvements between the full model and single-component ablations correspond to large effect sizes (Cohen’s $d > 0.8$), indicating that the gains are practically meaningful.

To illustrate the effects of the TST module and the contrastive loss, we compute the cosine similarity between slot representation vectors and visualize them as heat maps across frame sequences (Figure 6). When the TST module is disabled, temporal consistency deteriorates. As shown on the left side of the figure, the mask originally tracking the instrument on the left (slot index 0, blue mask) switches to another slot (index 2, green mask). Similarly, the tissue at the bottom, initially represented by a single slot (index 1), is later fragmented into two slots (indices 1 and 3). These inconsistencies are also evident in the similarity matrix, where pronounced fluctuations appear in the rows corresponding to these slots. In contrast, under the full Slot-BERT configuration, object tracking is more stable. For example, the same left instrument (slot index 6, purple mask) remains

consistently represented by a single slot across the entire sequence, which is reflected by the smoother, more stable row in the similarity matrix at the bottom.

The effect of removing the contrastive loss is shown on the right of Figure 6. In this setting, slot similarities remain uniformly high (above 0.6), whereas with contrastive loss they are pushed lower, clustering around zero, enforcing that slots encode diverging directions in the representation hyper-space. Without contrastive loss, the model exhibits segmentation instability: two distinct instruments in the lower-right region of the frame are merged into a single slot (index 4) across the video. This ambiguity is reflected in the similarity matrix as bright regions indicating high correlation between slot vectors. By contrast, when contrastive loss is applied, slots are explicitly encouraged to diverge, enabling the two neighboring instruments to be represented by separate slots (indices 1 and 3, shown in orange and red masks).

Figure 7 presents ablation results on three datasets with varying test-video lengths. We evaluate video-level accuracy (mBO-V) and temporal-slot IDF1, comparing the full method against variants with (w) or without (w/o) the contrastive objective and/or the TST module. Note that the Thoracic dataset is only partially and sparsely annotated; therefore, comparisons on this dataset are conducted only at full video length (30 frames).

Across all datasets, both contrastive learning and temporal self-training consistently improve surgical instrument segmentation and tracking. On the MICCAI dataset (11-frame sequences), adding contrastive learning alone improves mBO-V by approximately 3.6 percentage points over the baseline, while adding TST alone yields an improvement of approximately 5.1 points; combining both components results in a larger gain of approximately 6.7 points. Similar trends are observed across datasets and metrics, with combined gains of 3–7 points in mBO-V and 4–11 points in temporal slot IDF1.

Most of these improvements are statistically significant ($p < 0.0167$, with Bonferroni correction $m = 3$). An exception is observed for mBO-V on Cholec at 30 frames when comparing the full model to the TST-only variant, where the difference does not reach statistical significance ($p = 0.46$). This behavior likely reflects the increased difficulty of segmenting tissue and small instruments in Cholec videos. Importantly, even in this setting, the full model achieves significantly higher temporal slot IDF1 than the TST-only variant ($p < 0.01$), indicating stronger identity consistency. Taken together, these results confirm the complementary roles of contrastive learning and temporal self-training in robust surgical scene decomposition and long-range tracking.

Table 7. Performance comparison of Slot-Mixer decoder configurations on MICCAI and zero-shot Endovis benchmarks. The table presents results for three configurations: Mixer Only, Contrast+Mixer, and Slot-BERT+Mixer. The Slot-BERT+Mixer configuration consistently outperforms the others across both benchmarks, demonstrating that for the alternative decoders the proposed slot contrastive learning with TST module can enhance object-centric learning performance in video.

Setup	MICCAI			
	mBO-V	mBO-F	mBHD(\downarrow)	CorLoc
Mixer only	47.1±0.4	51.2±0.3	50.889±0.326	61.6±0.5
Contrast+Mixer	48.9±0.6	53.1±0.5	48.121±1.197	66.2±0.7
Mixer-full	49.0±0.4	53.2±0.2	46.994±1.008	67.4±0.9
Setup	Zero shot to Endovis			
	mBO-V	mBO-F	mBHD (\downarrow)	CorLoc
Mixer only	42.7±0.3	47.1±0.2	54.321±0.6	58.1±0.6
Contrast+Mixer	43.3±0.1	47.5±0.2	53.021±0.279	60.9±1.1
Mixer-full	43.2±0.2	47.5±0.2	51.945±0.5	61.9±0.3

4.10. Contrastive hyperparameter tuning analysis

To investigate the effect of contrastive loss hyper-parameters on model performance, we systematically varied the contrastive loss weight (α) from 0.0001 to 0.1 and the temperature parameter (τ) from 0.05 to 100. Figure 8 visualizes the tendency.

Overall, we observe that a larger contrastive weight (e.g., $\alpha = 0.1$) requires a higher temperature to achieve better accuracy. This is likely because over-enforcing a strong dissimilarity between slots can have negative impact on object-centric learning; a higher temperature effectively smooths the contrastive distribution, mitigating the over-penalization caused by large weights. Conversely, when the contrastive weight is too small (e.g., $\alpha = 10^{-4}$), the effect of varying the temperature is marginal, as the relative change of influence on training dynamics is much less for this combination.

These findings suggest that a moderate weight on the contrastive objective, coupled with a balanced temperature scaling, provides the best trade-off between encouraging slot diversity and maintaining stable optimization. In particular, tuning the parameters to $\alpha = 0.01$ and $\tau = 0.5$ yields the highest video-level segmentation performance, achieving 50.1 mBO-V, which represents a notable improvement over the baseline model without contrastive learning (46.3 mBO-V).

4.11. Experiment with Slot-Mixer decoder

To evaluate our method with the alternative Slot-Mixer decoder (Zadaianchuk et al., 2023), we conducted experiments using the Slot-BERT framework and compared it against two additional configurations. The results are reported for the MICCAI benchmark, where the model is trained and tested on MICCAI, and the zero-shot Endovis

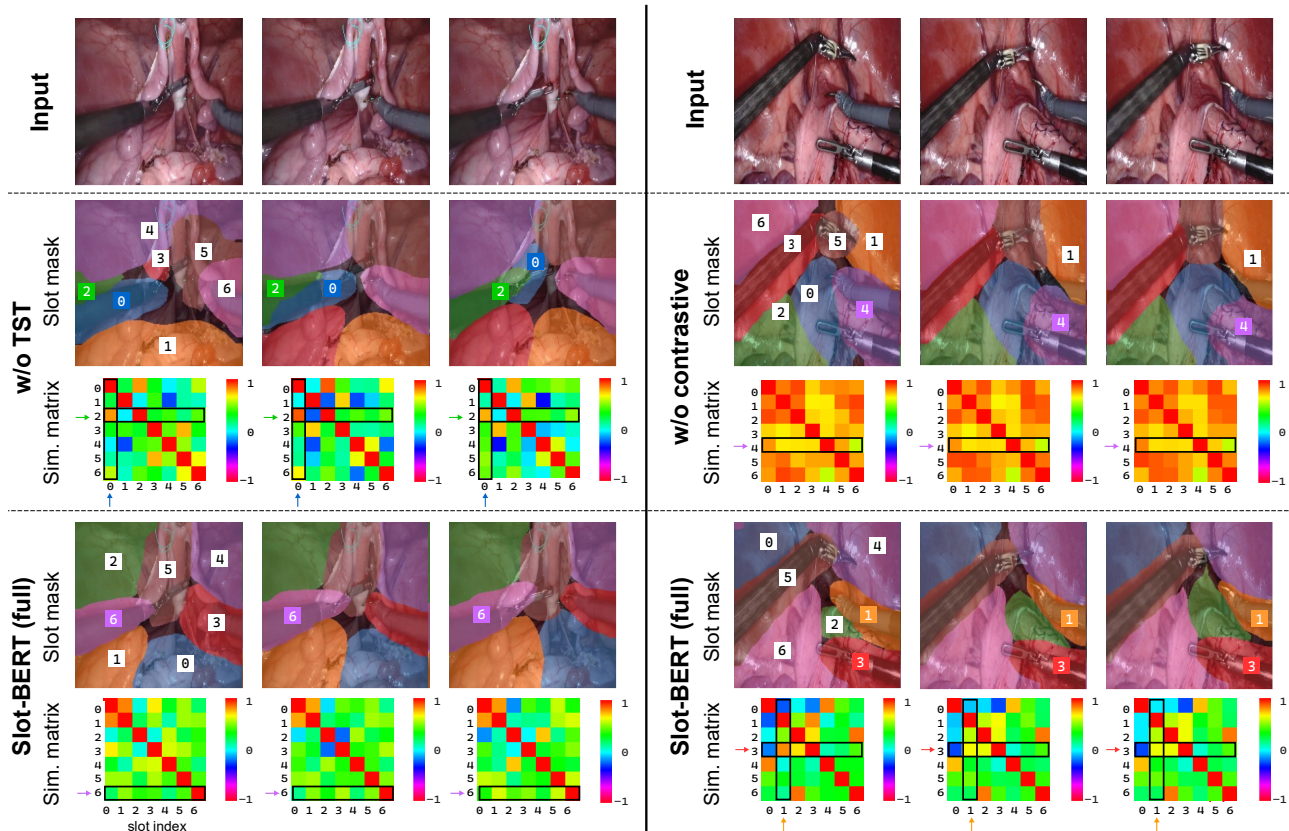


Figure 6. Slot masks and the corresponding cosine similarity matrices for Slot-BERT and ablated Slot-BERT variants without the TST module (left) or contrastive loss (right). All models are trained with 7 slots, and each segmentation mask is annotated with its corresponding slot index (0-6). See text for details.

benchmark, where the model trained on MICCAI is tested directly on Endovis without fine-tuning. The first configuration, **Mixer Only**, combines a vanilla RNN Slot Attention with the Slot Mixer for feature reconstruction. The second, **Contrast+Mixer**, incorporates slot contrastive loss into the training process while still relying on the Slot-Mixer for decoding. Finally, **Mixer-full** represents the full proposed method.

As shown in table 7, in the MICCAI benchmark, the proposed method achieves an mBHD error of 46.9, improving upon the results of baseline of Mixer-only 50.8. For Endovis, in zero-shot transfer, our method achieves mBHD of 51.9. This demonstrates the comparable performance of the Slot-Mixer decoder to the MLP decoder: 44.2 mBHD on MICCAI and 50.7 mBHD zero shot to Endovis (table 2 and table 4).

These findings confirm that our method is able to surpass the vanilla RNN-based baseline using either MLP broadcast, or Slot-Mixer decoder which improves decoding quality by introducing interactions between slots, achieving high localization and segmentation performance. For more qualitative results refer to the section 1.1 of supplementary materials.

4.12. Affect of the amount of training data on performance

We evaluate the sensitivity of segmentation performance to the amount of training data. Figure 9 compares Slot-BERT, our proposed method, with Video-Saur on the MICCAI challenge dataset, using mBO-V as video-level segmentation accuracy evaluation metrics. Training data proportions range from the full dataset (1.0) to 1% (0.01).

Slot-BERT demonstrates remarkable robustness in dealing with a decrease in training data. With the full dataset, it achieves 48.9% accuracy compared to 46.3% for Video-Saur. With only 30% of the data, Slot-BERT maintains 47.5%, nearly matching its full training data performance, while Video-Saur drops to 44.4%. At lower data ratios, the gap widens significantly: Slot-BERT achieves 30.4% at 0.05 compared to Video-Saur’s 7.3%, and at 0.01, Slot-BERT retains 19.6% while Video-Saur falls to 6.0%. In summary, Slot-BERT consistently outperforms Video-Saur across all data proportions and maintains higher accuracy even with minimal data. Its graceful degradation in performance highlights its robustness and makes it particularly effective for segmentation tasks in data-scarce scenarios.

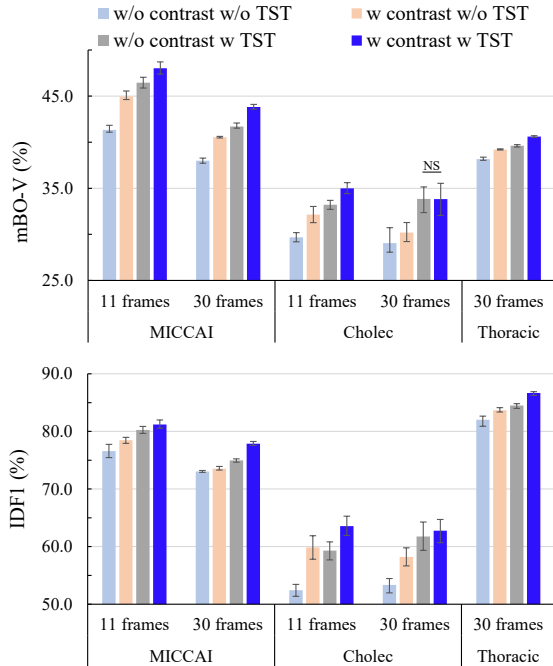


Figure 7. Ablation study on three datasets with varying test video lengths. We compare video-level segmentation accuracy (mBO-V) and the temporal slot IDF1 score. Our full method is evaluated against variants with (w) or without (w/o) the slot contrastive learning objective and the TST module. Note that the Thoracic dataset is only partially and sparsely annotated; therefore, comparisons on this dataset are conducted only using the full video length (30 frames).

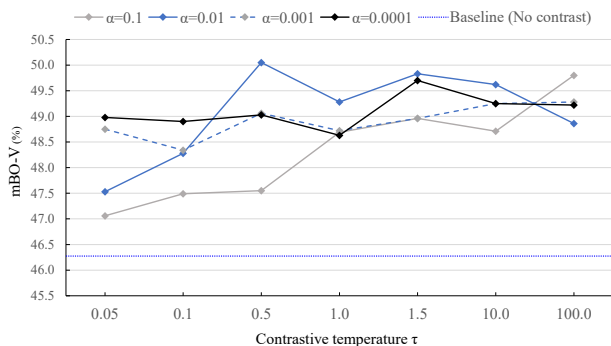


Figure 8. Parameter tuning of Slot-BERT with respect to contrastive loss weight (α) and temperature (τ). Performance is reported as mBO-V. Across a range of α values (0.0001-0.1) and τ values (0.05-100), we observe consistent improvement compared to the baseline without contrastive learning. The best performance is achieved with $\alpha = 0.01$ and $\tau = 0.5$, reaching 50.1 mBO-V, highlighting the importance of jointly balancing temperature scaling and loss weighting.

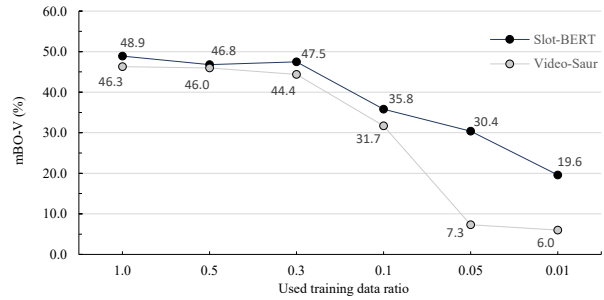


Figure 9. Comparison of Slot-BERT and Video-Saur performance as a function of training data proportion. The evaluation metrics is mBO-V (video-level segmentation accuracy), with data proportions ranging from the full dataset (1.0) to 1% (0.01). Slot-BERT demonstrates much higher accuracy (20.8 vs 6.1 mBO-V) even with minimal training data, whereas Video-Saur’s performance significantly drops as data decreases.

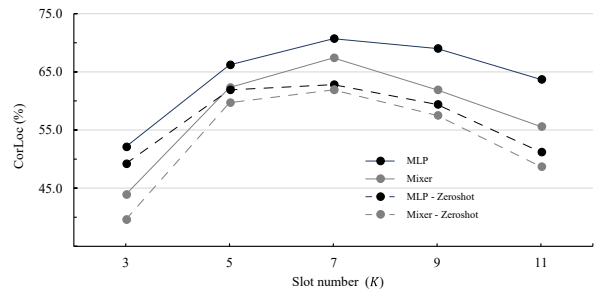


Figure 10. Object localization accuracy (CorLoc) with varying slot numbers (K). This figure presents the effect of changing the number of slots (K) on object localization accuracy, comparing performance on both the training domain and zero-shot data. The results show that $K = 7$ yields the best performance for both the MLP and Mixer decoders.

4.13. Experiment with different slot numbers

In order to investigate the effect of changing slot number K on the performance of Slot-BERT, experiments were conducted using MLP and Mixer decoders. Figure 10 presents the CorLoc score obtained on training domain and zero-shot data, to evaluate impact of slot allocation on the localization accuracy. The results show that $K = 7$ generally provides the best performance for both methods, with MLP achieving a peak score of 70.7 and Mixer reaching 67.4 on training domain data. As K increases beyond 7, performance begins to decline for both decoders, suggesting that excessively large K values might over-delineate the image as the number of objects in a video is limited. MLP consistently outperforms Mixer on training domain data, indicating its superior ability to leverage increased K for improved predictions.

On zero-shot data, the trend remains consistent, with both MLP and Mixer achieving their best scores at $K = 7$, though their overall performance is lower compared to the

Table 8. Runtime and computational cost comparison in terms of per-frame inference time and GFLOPs. Best results are highlighted in bold.

Method	Time per frame (ms)	GFLOPs
SAVi(Kipf et al., 2022)	3.3	430.677
STEVE(Singh et al., 2022)	8.2	540.701
Slot-Diffusion(Wu et al., 2023b)	5.7	334.196
Video-Saur(Zadaianchuk et al., 2023)	1.2	411.703
Slot-BERT (ours)	1.7	453.450

training domain. MLP slightly outperforms Mixer across most K values, reaching a maximum zero-shot score of 62.8, compared to Mixer’s 61.9 at $K = 7$. These results highlight that while $K = 7$ is optimal across both datasets, there is a clear performance gap between training domain and zeroshot data, reflecting challenges in generalization. The analysis demonstrates that adjusting K significantly impacts the effectiveness of both decoding methods, emphasizing the importance of finding an optimal K value to balance performance and generalization. Evaluation of different slot number under additional metrics are concluded in Supplementary Material section E.

4.14. Computational efficiency analysis

We benchmark the computational efficiency of Slot-BERT against existing object-centric video models. The forward inference time per frame is measured on a single NVIDIA RTX A6000 GPU using video clips of 30 seconds, where we set the temporal context window to 5 seconds. We also report the floating point operations per second (GFLOPs), which quantify the computational cost of processing a single frame. The slot number for all methods is set to 7 in this experiment.

As shown in Table 8, Video-Saur achieves the fastest inference speed (1.2 ms per frame), while Slot-BERT maintains a competitive runtime efficiency (1.7 ms per frame) with only a minor computational overhead compared to other baselines. Although Slot-Diffusion reports the lowest GFLOPs (334.196), its inference speed is not competitive due to the iterative nature of diffusion-based decoding process.

We also evaluated the memory consumption under real-time video processing with slot mixer decoder. In this setting, the RNN-based model, Video-Saur requires 369.32 MB. By incorporating TST module With a 5-frame context window, the overhead of slot-BERT is only 1.69 MB (371.01 MB total), and with a 30-frame context window, the overhead remains modest at 2.09 MB, thanks to the latent space operation of temporal attention.

4.15. Experiment with different context window lengths

To analyze the trade-off between temporal context length, segmentation accuracy, and computational efficiency, we

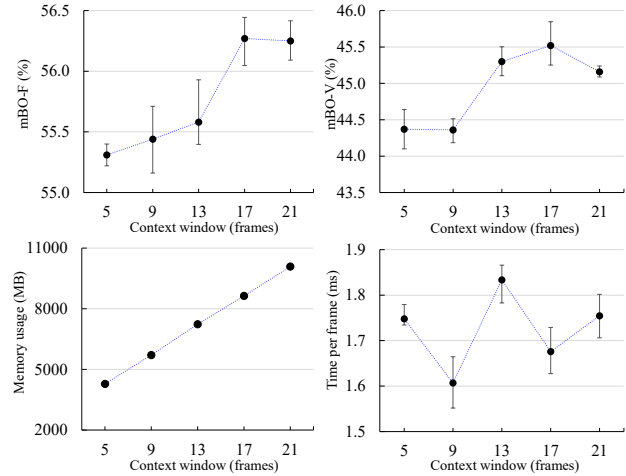


Figure 11. Benchmark of our method using context window sizes ranging from 5 to 21 frames, evaluated on videos of fixed length (30 frames). Frame-level accuracy (mBO-F), video-level accuracy (mBO-V), GPU memory usage, and per-frame forward inference time are compared across different context window sizes.

experiment with different context window lengths, ranging from 5 to 21 frames, while processing videos of fixed length (30 frames). As shown in Fig. 11, increasing the context window leads to up to 1% improvements in both frame-level accuracy (mBO-F) and video-level accuracy (mBO-V), indicating that longer temporal context enhances reasoning over object dynamics.

The performance gains are most pronounced when increasing the context window from 5 to 13 frames for the video-level metric mBO-V, which reflects a steady improvement in temporal consistency across frames. When the context window is further extended to 17 and 21 frames, the accuracy improvements begin to saturate, suggesting diminishing returns.

In contrast, the computational cost increases approximately linearly with the context window length, as reflected by the steady growth in GPU memory consumption. The per-frame inference time remains largely stable (around 1.7 ms) across different window lengths, indicating that the TST module introduces only minimal additional computational latency as the temporal context expands. The variations in per-frame runtime are thus driven by factors such as GPU parallelization and system-level scheduling rather than the choice of context window.

Overall, this experiment highlights a clear accuracy-efficiency trade-off guiding the selection of context window length. On our datasets, a moderate context window (e.g., 9-13 frames) provides a favorable balance for unsupervised video segmentation, achieving most of the attainable accuracy gains while maintaining low memory overhead.

At 1 FPS, the context window duration is between 9 to 13 seconds and this length seems to capture well the dynamics of instruments and tissue in surgery. Ultimately, the method is adaptable to different application scenarios and computational constraints.

5. Conclusions

Slot-BERT demonstrated robust spatial segmentation and temporal reasoning capabilities, achieving state-of-the-art results across diverse datasets. The proposed bidirectional slots transformer enabled reasoning over video sequences without the scalability issues typical of parallel methods, because the attention operates on lightweight slot embeddings. This capability is particularly relevant for domains requiring long-term temporal coherence, such as surgical video analysis.

By enforcing orthogonality between slots, our contrastive loss improved the independence of latent representations, reducing leakage across slot boundaries. This enhancement translated into more precise segmentation maps and improved object discovery, even in zero-shot settings.

Unlike existing models that either simply update slots recursively, lacking long-range reasoning, or process entire video features for grouping, which is computationally costly, **Slot-BERT** scales efficiently for videos. It achieves competitive performance without relying on computationally intensive modalities like optical flow or depth maps. This characteristic makes **Slot-BERT** a practical choice for real-world applications requiring affordable computational resources.

5.1. Limitations

The effectiveness of slot-based representations partially depends on the quality of initial slot assignments. Suboptimal initialization can impact downstream temporal reasoning and segmentation quality. The number of slots also plays a role in how well slots encompass particular object instances. The optimal number of slots, as well as dynamic slot allocation are part of current research (Fan et al., 2024).

Although effective in handling moderate temporal dynamics, scenarios involving rapid, non-linear object motion or occlusions may still present challenges for **Slot-BERT**. Object exit from and re-entry into the field of view remains a fundamental challenge for fully unsupervised, online object-centric tracking. When an object disappears, its corresponding slot may be reassigned to background regions. Upon reappearance, there is no explicit supervision to guarantee reassociation with the original slot, particularly under prolonged occlusion or appearance change. Addressing this limitation may require incorporating memory mechanisms or weak supervision (Nwoye et al., 2019; Liao et al., 2025).

While our model outperformed baselines in zero-shot generalization tasks, there is room for improvement in handling novel object classes or extreme domain shifts.

While our model discovers the overall location and shape of objects, it fails to predict the exact pixel-level boundaries, lowering the semantic segmentation accuracy. This is partially due to patch-based processing and could be mitigated by increasing the resolution of the patch grid. The model trained on lower-resolution path features can serve as guidance for higher-resolution modalities, such as optical flow and image saliency maps, enabling accurate high-resolution segmentation in an unsupervised manner. With **Slot-BERT** the stability of integrating these modalities will be enhanced.

5.2. Future Directions

Incorporating additional priors or augmentations for slot initialization, such as unsupervised identifiable slot attention mechanisms (Kori et al., 2024), may further enhance segmentation and temporal reasoning capabilities. Slot attention is a fully un-supervised representation learning algorithm; however, it can also be implemented in weakly supervised learning or in a human-interactive manner to identify the class of each slot so that pseudo-segmentation masks can be generated. Specifically, with weak video class labels, set prediction frameworks can be adopted to the latent space of slots (Sun et al., 2021). Alternatively, with pre-trained slot models, annotators only need to identify which slot needs to be tracked or which slot represents the object of interest. In such interactive implementations, **Slot-BERT** can reduce the annotation burden in labeling tasks or directly serve as an attention aid in tasks like surgical tracking and planning.

While **Slot-BERT** eschews computationally intensive modalities like optical flow or feature similarity, integrating lightweight versions of these signals could provide complementary information in challenging scenarios. Such modalities could be an option to increase the resolution of slot attention masks, which are currently limited by the resolution of patches. For instance, the similarity of images or lower-level features often has much higher resolution compared to high-level features.

Beyond incorporating additional modalities such as optical flow or depth maps to refine boundary accuracy, another promising direction is domain-specific high-resolution fine-tuning. This could be achieved by leveraging models pretrained on lower-resolution inputs (as typically required by default backbones like DINO) as anchors for adaptation (Didolkar et al., 2025). In addition, DINOv3 (Siméoni et al., 2025) that is already trained with a high-resolution adaptation phase supports effective inference using high-resolution features.

Extending [Slot-BERT](#) to other biomedical domains, such as surgical videos involving cell segmentation in microscopic volumes or organ segmentation in MRI scanning sequences, would help evaluate its adaptability to diverse tasks.

[Slot-BERT](#) represents a significant advancement in object-centric video representation learning, addressing critical challenges in long video sequences of surgical domains. By integrating slot-based reasoning with bidirectional transformers, the model balances scalability and segmentation accuracy, paving the way for future innovations in self-supervised learning. Its demonstrated potential for zero-shot generalization highlights the importance of modular, explainable architectures for tackling real-world, domain-specific challenges.

Acknowledgments

This work was supported by the University of Pennsylvania Thomas B. McCabe and Jeannette E. Laws McCabe Fellow Award and the Linda Pechenik Montague Investigator Award.

References

- Arnab, A., Dehghani, M., Heigold, G., Sun, C., Lucic, M., and Schmid, C. Vivit: A video vision transformer. In *2021 IEEE/CVF International Conference on Computer Vision, ICCV 2021, Montreal, QC, Canada, October 10-17, 2021*, pp. 6816–6826, 2021.
- Assran, M., Caron, M., Misra, I., Bojanowski, P., Bordes, F., Vincent, P., Joulin, A., Rabbat, M., and Ballas, N. Masked siamese networks for label-efficient learning. In *European Conference on Computer Vision*, pp. 456–473. Springer, 2022.
- Aydemir, G., Xie, W., and Güney, F. Self-supervised object-centric learning for videos. In *Advances in Neural Information Processing Systems 36: Annual Conference on Neural Information Processing Systems 2023, NeurIPS 2023, New Orleans, LA, USA, December 10 - 16, 2023*, 2023.
- Bao, H., Dong, L., Piao, S., and Wei, F. Beit: BERT pre-training of image transformers. In *The Tenth International Conference on Learning Representations, ICLR 2022, Virtual Event, April 25-29, 2022*, 2022a.
- Bao, Z., Tokmakov, P., Jabri, A., Wang, Y., Gaidon, A., and Hebert, M. Discovering objects that can move. In *IEEE/CVF Conference on Computer Vision and Pattern Recognition, CVPR 2022, New Orleans, LA, USA, June 18-24, 2022*, pp. 11779–11788, 2022b.
- Bao, Z., Tokmakov, P., Wang, Y., Gaidon, A., and Hebert, M. Object discovery from motion-guided tokens. In *IEEE/CVF Conference on Computer Vision and Pattern Recognition, CVPR 2023, Vancouver, BC, Canada, June 17-24, 2023*, pp. 22972–22981, 2023.
- Bilen, H. and Vedaldi, A. Weakly supervised deep detection networks. In *2016 IEEE Conference on Computer Vision and Pattern Recognition, CVPR 2016, Las Vegas, NV, USA, June 27-30, 2016*, pp. 2846–2854, 2016.
- Biza, O., van Steenkiste, S., Sajjadi, M. S. M., Elsayed, G. F., Mahendran, A., and Kipf, T. Invariant slot attention: Object discovery with slot-centric reference frames. In *International Conference on Machine Learning, ICML 2023, 23-29 July 2023, Honolulu, Hawaii, USA*, volume 202 of *Proceedings of Machine Learning Research*, pp. 2507–2527, 2023.
- Burgess, C. P., Matthey, L., Watters, N., Kabra, R., Higgins, I., Botvinick, M., and Lerchner, A. Monet: Unsupervised scene decomposition and representation. *ArXiv preprint*, abs/1901.11390, 2019.
- Caron, M., Touvron, H., Misra, I., Jégou, H., Mairal, J., Bojanowski, P., and Joulin, A. Emerging properties in self-supervised vision transformers. In *2021 IEEE/CVF International Conference on Computer Vision, ICCV 2021, Montreal, QC, Canada, October 10-17, 2021*, pp. 9630–9640, 2021.
- Chen, M., Radford, A., Child, R., Wu, J., Jun, H., Luan, D., and Sutskever, I. Generative pretraining from pixels. In *Proceedings of the 37th International Conference on Machine Learning, ICML 2020, 13-18 July 2020, Virtual Event*, volume 119 of *Proceedings of Machine Learning Research*, pp. 1691–1703, 2020a.
- Chen, T., Kornblith, S., Norouzi, M., and Hinton, G. E. A simple framework for contrastive learning of visual representations. In *Proceedings of the 37th International Conference on Machine Learning, ICML 2020, 13-18 July 2020, Virtual Event*, volume 119 of *Proceedings of Machine Learning Research*, pp. 1597–1607, 2020b.
- Chen, X., Xie, S., and He, K. An empirical study of training self-supervised vision transformers. In *2021 IEEE/CVF International Conference on Computer Vision, ICCV 2021, Montreal, QC, Canada, October 10-17, 2021*, pp. 9620–9629, 2021.
- Cheng, H. K., Oh, S. W., Price, B., Schwing, A. G., and Lee, J. Tracking anything with decoupled video segmentation. In *IEEE/CVF International Conference on Computer Vision, ICCV 2023, Paris, France, October 1-6, 2023*, pp. 1316–1326, 2023.
- Choudhury, S., Karazija, L., Laina, I., Vedaldi, A., and Ruppel, C. Guess what moves: Unsupervised video

-
- and image segmentation by anticipating motion. In *33rd British Machine Vision Conference 2022, BMVC 2022, London, UK, November 21-24, 2022*, pp. 554, 2022.
- Croitoru, I., Bogolin, S.-V., and Leordeanu, M. Unsupervised learning of foreground object segmentation. *International Journal of Computer Vision*, 127:1279–1302, 2019.
- Devlin, J., Chang, M.-W., Lee, K., and Toutanova, K. BERT: Pre-training of deep bidirectional transformers for language understanding. In *Proceedings of the 2019 Conference of the North American Chapter of the Association for Computational Linguistics: Human Language Technologies, Volume 1 (Long and Short Papers)*, pp. 4171–4186, 2019.
- Didolkar, A., Zadaianchuk, A., Goyal, A., Mozer, M., Bengio, Y., Martius, G., and Seitzer, M. On the transfer of object-centric representation learning. In *International Conference on Learning Representations (ICLR)*, 2025. URL <https://arxiv.org/abs/2408.09162>.
- Dong, X., Bao, J., Zhang, T., Chen, D., Zhang, W., Yuan, L., Chen, D., Wen, F., Yu, N., and Guo, B. Peco: Perceptual codebook for BERT pre-training of vision transformers. In *Thirty-Seventh AAAI Conference on Artificial Intelligence, AAAI 2023, Thirty-Fifth Conference on Innovative Applications of Artificial Intelligence, IAAI 2023, Thirteenth Symposium on Educational Advances in Artificial Intelligence, EAAI 2023, Washington, DC, USA, February 7-14, 2023*, pp. 552–560, 2023.
- Dosovitskiy, A., Beyer, L., Kolesnikov, A., Weissenborn, D., Zhai, X., Unterthiner, T., Dehghani, M., Minderer, M., Heigold, G., Gelly, S., Uszkoreit, J., and Hounsby, N. An image is worth 16x16 words: Transformers for image recognition at scale. In *9th International Conference on Learning Representations, ICLR 2021, Virtual Event, Austria, May 3-7, 2021*, 2021.
- Eastwood, C. and Williams, C. K. I. A framework for the quantitative evaluation of disentangled representations. In *6th International Conference on Learning Representations, ICLR 2018, Vancouver, BC, Canada, April 30 - May 3, 2018, Conference Track Proceedings*, 2018.
- Elsayed, G. F., Mahendran, A., van Steenkiste, S., Greff, K., Mozer, M. C., and Kipf, T. Savi++: Towards end-to-end object-centric learning from real-world videos. In *Advances in Neural Information Processing Systems 35: Annual Conference on Neural Information Processing Systems 2022, NeurIPS 2022, New Orleans, LA, USA, November 28 - December 9, 2022*, 2022.
- Engelcke, M., Kosiorek, A. R., Jones, O. P., and Posner, I. GENESIS: generative scene inference and sampling with object-centric latent representations. In *8th International Conference on Learning Representations, ICLR 2020, Addis Ababa, Ethiopia, April 26-30, 2020*, 2020.
- Fan, K., Bai, Z., Xiao, T., He, T., Horn, M., Fu, Y., Locatello, F., and Zhang, Z. Adaptive slot attention: Object discovery with dynamic slot number. In *Proceedings of the IEEE/CVF Conference on Computer Vision and Pattern Recognition*, pp. 23062–23071, 2024.
- Fragkiadaki, K., Arbelaez, P., Felsen, P., and Malik, J. Learning to segment moving objects in videos. In *IEEE Conference on Computer Vision and Pattern Recognition, CVPR 2015, Boston, MA, USA, June 7-12, 2015*, pp. 4083–4090, 2015.
- Greff, K., Kaufman, R. L., Kabra, R., Watters, N., Burgess, C., Zoran, D., Matthey, L., Botvinick, M., and Lerchner, A. Multi-object representation learning with iterative variational inference. In *Proceedings of the 36th International Conference on Machine Learning, ICML 2019, 9-15 June 2019, Long Beach, California, USA*, volume 97 of *Proceedings of Machine Learning Research*, pp. 2424–2433, 2019.
- Greff, K., Van Steenkiste, S., and Schmidhuber, J. On the binding problem in artificial neural networks. *ArXiv preprint*, abs/2012.05208, 2020.
- Greff, K., Minderer, M., Papamakarios, G., Engelcke, M., Hennigan, T., Buhmann, J. M., Doucet, A., Murphy, K., Arbeláez, P., Oliver, N., Beattie, C., Gamper, H., Malinowski, M., Gelly, S., Unther, M., Kipf, T., and Dosovitskiy, A. Kubric: A scalable dataset generator. In *Proceedings of the IEEE/CVF Conference on Computer Vision and Pattern Recognition (CVPR)*, pp. 3749–3761, 2022.
- He, K., Chen, X., Xie, S., Li, Y., Dollár, P., and Girshick, R. B. Masked autoencoders are scalable vision learners. In *IEEE/CVF Conference on Computer Vision and Pattern Recognition, CVPR 2022, New Orleans, LA, USA, June 18-24, 2022*, pp. 15979–15988, 2022.
- Hénaff, O. J., Koppula, S., Shelhamer, E., Zoran, D., Jaegle, A., Zisserman, A., Carreira, J., and Arandjelović, R. Object discovery and representation networks. In *European conference on computer vision*, pp. 123–143. Springer, 2022.
- Higgins, I., Matthey, L., Pal, A., Burgess, C., Glorot, X., Botvinick, M., Mohamed, S., and Lerchner, A. beta-vae: Learning basic visual concepts with a constrained variational framework. In *5th International Conference on Learning Representations, ICLR 2017, Toulon, France, April 24-26, 2017, Conference Track Proceedings*, 2017.

-
- Hinton, G. E., Sabour, S., and Frosst, N. Matrix capsules with EM routing. In *6th International Conference on Learning Representations, ICLR 2018, Vancouver, BC, Canada, April 30 - May 3, 2018, Conference Track Proceedings*, 2018.
- Hong, W.-Y., Kao, C.-L., Kuo, Y.-H., Wang, J.-R., Chang, W.-L., and Shih, C.-S. Cholecseg8k: a semantic segmentation dataset for laparoscopic cholecystectomy based on cholec80. *ArXiv preprint*, abs/2012.12453, 2020.
- Hou, Q., Jiang, P., Wei, Y., and Cheng, M. Self-erasing network for integral object attention. In *Advances in Neural Information Processing Systems 31: Annual Conference on Neural Information Processing Systems 2018, NeurIPS 2018, December 3-8, 2018, Montréal, Canada*, pp. 547–557, 2018.
- Ibrahim, M., Akhtar, N., Anwar, S., and Mian, A. Sat3d: Slot attention transformer for 3d point cloud semantic segmentation. *IEEE Transactions on Intelligent Transportation Systems*, 24(5):5456–5466, 2023.
- Jiang, J., Deng, F., Singh, G., and Ahn, S. Object-centric slot diffusion. In *Advances in Neural Information Processing Systems 36: Annual Conference on Neural Information Processing Systems 2023, NeurIPS 2023, New Orleans, LA, USA, December 10 - 16, 2023*, 2023.
- Kahneman, D., Treisman, A., and Gibbs, B. J. The reviewing of object files: Object-specific integration of information. *Cognitive psychology*, 24(2):175–219, 1992.
- Karazija, L., Choudhury, S., Laina, I., Rupprecht, C., and Vedaldi, A. Unsupervised multi-object segmentation by predicting probable motion patterns. In *Advances in Neural Information Processing Systems 35: Annual Conference on Neural Information Processing Systems 2022, NeurIPS 2022, New Orleans, LA, USA, November 28 - December 9, 2022*, 2022.
- Kim, H. and Mnih, A. Disentangling by factorising. In *Proceedings of the 35th International Conference on Machine Learning, ICML 2018, Stockholmsmässan, Stockholm, Sweden, July 10-15, 2018*, volume 80 of *Proceedings of Machine Learning Research*, pp. 2654–2663, 2018.
- Kingma, D. P. and Welling, M. Auto-encoding variational bayes. In *2nd International Conference on Learning Representations, ICLR 2014, Banff, AB, Canada, April 14-16, 2014, Conference Track Proceedings*, 2014.
- Kipf, T., Elsayed, G. F., Mahendran, A., Stone, A., Sabour, S., Heigold, G., Jonschkowski, R., Dosovitskiy, A., and Greff, K. Conditional object-centric learning from video. In *The Tenth International Conference on Learning Representations, ICLR 2022, Virtual Event, April 25-29, 2022*, 2022.
- Kipf, T. N., van der Pol, E., and Welling, M. Contrastive learning of structured world models. In *8th International Conference on Learning Representations, ICLR 2020, Addis Ababa, Ethiopia, April 26-30, 2020*, 2020.
- Kori, A., Locatello, F., Santhirasekaram, A., Toni, F., Glocker, B., and Ribeiro, F. D. S. Identifiable object-centric representation learning via probabilistic slot attention. *Advances in Neural Information Processing Systems*, 2024.
- Kossen, J., Stelzner, K., Hussing, M., Voelcker, C., and Kersting, K. Structured object-aware physics prediction for video modeling and planning. In *8th International Conference on Learning Representations, ICLR 2020, Addis Ababa, Ethiopia, April 26-30, 2020*, 2020.
- Lee, J., Kim, E., Lee, S., Lee, J., and Yoon, S. Ficklenet: Weakly and semi-supervised semantic image segmentation using stochastic inference. In *IEEE Conference on Computer Vision and Pattern Recognition, CVPR 2019, Long Beach, CA, USA, June 16-20, 2019*, pp. 5267–5276, 2019.
- Lee, M., Cho, S., Lee, D., Park, C., Lee, J., and Lee, S. Guided slot attention for unsupervised video object segmentation. In *Proceedings of the IEEE/CVF Conference on Computer Vision and Pattern Recognition*, pp. 3807–3816, 2024.
- Liao, G., Jogan, M., Koushik, S., Eaton, E., and Hashimoto, D. A. Disentangling spatio-temporal knowledge for weakly supervised object detection and segmentation in surgical video. *ArXiv preprint*, abs/2407.15794, 2024.
- Liao, G., Jogan, M., Koushik, S., Eaton, E., and Hashimoto, D. A. Disentangling spatio-temporal knowledge for weakly supervised object detection and segmentation in surgical video. In *2025 IEEE/CVF Winter Conference on Applications of Computer Vision (WACV)*, pp. 8013–8023. IEEE, 2025.
- Lin, Z., Wu, Y., Peri, S. V., Sun, W., Singh, G., Deng, F., Jiang, J., and Ahn, S. SPACE: unsupervised object-oriented scene representation via spatial attention and decomposition. In *8th International Conference on Learning Representations, ICLR 2020, Addis Ababa, Ethiopia, April 26-30, 2020*, 2020.
- Liu, R., Wu, Z., Yu, S. X., and Lin, S. The emergence of objectness: Learning zero-shot segmentation from videos. In *Advances in Neural Information Processing Systems*

-
- 34: *Annual Conference on Neural Information Processing Systems 2021, NeurIPS 2021, December 6-14, 2021, virtual*, pp. 13137–13152, 2021.
- Locatello, F., Weissenborn, D., Unterthiner, T., Mahendran, A., Heigold, G., Uszkoreit, J., Dosovitskiy, A., and Kipf, T. Object-centric learning with slot attention. In *Advances in Neural Information Processing Systems 33: Annual Conference on Neural Information Processing Systems 2020, NeurIPS 2020, December 6-12, 2020, virtual*, 2020.
- Löwe, S., Lippe, P., Rudolph, M., Welling, M., et al. Complex-valued autoencoders for object discovery. *Transactions on Machine Learning Research*, (428), 2022.
- Mansouri, A., Hartford, J., Zhang, Y., and Bengio, Y. Object-centric architectures enable efficient causal representation learning. *ArXiv preprint*, abs/2310.19054, 2023.
- Mathieu, E., Rainforth, T., Siddharth, N., and Teh, Y. W. Disentangling disentanglement in variational autoencoders. In *Proceedings of the 36th International Conference on Machine Learning, ICML 2019, 9-15 June 2019, Long Beach, California, USA*, volume 97 of *Proceedings of Machine Learning Research*, pp. 4402–4412, 2019.
- Milan, A., Leal-Taixé, L., Reid, I., Roth, S., and Schindler, K. Mot16: A benchmark for multi-object tracking. In *CVPR*, 2016.
- Nwoye, C. I., Mutter, D., Marescaux, J., and Padoy, N. Weakly supervised convolutional lstm approach for tool tracking in laparoscopic videos. *International journal of computer assisted radiology and surgery*, 14(6):1059–1067, 2019.
- Ponimatkin, G., Samet, N., Xiao, Y., Du, Y., Marlet, R., and Lepetit, V. A simple and powerful global optimization for unsupervised video object segmentation. In *Proceedings of the IEEE/CVF Winter Conference on Applications of Computer Vision*, pp. 5892–5903, 2023.
- Pont-Tuset, J., Arbelaez, P., Barron, J. T., Marques, F., and Malik, J. Multiscale combinatorial grouping for image segmentation and object proposal generation. *IEEE transactions on pattern analysis and machine intelligence*, 39(1):128–140, 2016.
- Qian, R., Ding, S., Liu, X., and Lin, D. Semantics meets temporal correspondence: Self-supervised object-centric learning in videos. In *IEEE/CVF International Conference on Computer Vision, ICCV 2023, Paris, France, October 1-6, 2023*, pp. 16629–16641, 2023.
- Radford, A. Improving language understanding by generative pre-training. 2018.
- Radford, A., Kim, J. W., Hallacy, C., Ramesh, A., Goh, G., Agarwal, S., Sastry, G., Askell, A., Mishkin, P., Clark, J., Krueger, G., and Sutskever, I. Learning transferable visual models from natural language supervision. In *Proceedings of the 38th International Conference on Machine Learning, ICML 2021, 18-24 July 2021, Virtual Event*, volume 139 of *Proceedings of Machine Learning Research*, pp. 8748–8763, 2021.
- Ramesh, A., Pavlov, M., Goh, G., Gray, S., Voss, C., Radford, A., Chen, M., and Sutskever, I. Zero-shot text-to-image generation. In *Proceedings of the 38th International Conference on Machine Learning, ICML 2021, 18-24 July 2021, Virtual Event*, volume 139 of *Proceedings of Machine Learning Research*, pp. 8821–8831, 2021.
- Ristani, E., Solera, F., Zou, R., Cucchiara, R., and Tomasi, C. Performance measures and a data set for multi-target, multi-camera tracking. In *European Conference on Computer Vision (ECCV)*, 2016.
- Rombach, R., Blattmann, A., Lorenz, D., Esser, P., and Ommer, B. High-resolution image synthesis with latent diffusion models. In *Proceedings of the IEEE/CVF conference on computer vision and pattern recognition*, pp. 10684–10695, 2022.
- Sabour, S., Frosst, N., and Hinton, G. E. Dynamic routing between capsules. In *Advances in Neural Information Processing Systems 30: Annual Conference on Neural Information Processing Systems 2017, December 4-9, 2017, Long Beach, CA, USA*, pp. 3856–3866, 2017.
- Sajjadi, M. S. M., Duckworth, D., Mahendran, A., van Steenkiste, S., Pavetic, F., Lucic, M., Guibas, L. J., Greff, K., and Kipf, T. Object scene representation transformer. In *Advances in Neural Information Processing Systems 35: Annual Conference on Neural Information Processing Systems 2022, NeurIPS 2022, New Orleans, LA, USA, November 28 - December 9, 2022*, 2022.
- Seitzer, M., Horn, M., Zadaianchuk, A., Zietlow, D., Xiao, T., Simon-Gabriel, C., He, T., Zhang, Z., Schölkopf, B., Brox, T., and Locatello, F. Bridging the gap to real-world object-centric learning. In *The Eleventh International Conference on Learning Representations, ICLR 2023, Kigali, Rwanda, May 1-5, 2023*, 2023.
- Sestini, L., Rosa, B., De Momi, E., Ferrigno, G., and Padoy, N. Fun-sis: A fully unsupervised approach for surgical instrument segmentation. *Medical Image Analysis*, 85: 102751, 2023.
- Siméoni, O., Vo, H. V., Seitzer, M., Baldassarre, F., Oquab, M., Jose, C., Khalidov, V., Szafraniec, M., Yi, S., Ramamonjisoa, M., et al. Dinov3. *arXiv preprint arXiv:2508.10104*, 2025.

-
- Singh, G., Wu, Y., and Ahn, S. Simple unsupervised object-centric learning for complex and naturalistic videos. In *Advances in Neural Information Processing Systems 35: Annual Conference on Neural Information Processing Systems 2022, NeurIPS 2022, New Orleans, LA, USA, November 28 - December 9, 2022*, 2022.
- Singh, G., Wang, Y., Yang, J., Ivanovic, B., Ahn, S., Pavone, M., and Che, T. Parallelized spatiotemporal slot binding for videos. In *Forty-first International Conference on Machine Learning*, 2024.
- Sun, Z., Cao, S., Yang, Y., and Kitani, K. Rethinking transformer-based set prediction for object detection. In *2021 IEEE/CVF International Conference on Computer Vision, ICCV 2021, Montreal, QC, Canada, October 10-17, 2021*, pp. 3591–3600, 2021.
- Tenenbaum, J. B., Kemp, C., Griffiths, T. L., and Goodman, N. D. How to grow a mind: Statistics, structure, and abstraction. *science*, 331(6022):1279–1285, 2011.
- Tokmakov, P., Alahari, K., and Schmid, C. Learning motion patterns in videos. In *2017 IEEE Conference on Computer Vision and Pattern Recognition, CVPR 2017, Honolulu, HI, USA, July 21-26, 2017*, pp. 531–539, 2017.
- Tong, Z., Song, Y., Wang, J., and Wang, L. Videomae: Masked autoencoders are data-efficient learners for self-supervised video pre-training. In *Advances in Neural Information Processing Systems 35: Annual Conference on Neural Information Processing Systems 2022, NeurIPS 2022, New Orleans, LA, USA, November 28 - December 9, 2022*, 2022.
- Tsai, Y. H., Srivastava, N., Goh, H., and Salakhutdinov, R. Capsules with inverted dot-product attention routing. In *8th International Conference on Learning Representations, ICLR 2020, Addis Ababa, Ethiopia, April 26-30, 2020*, 2020.
- Twinanda, A. P., Shehata, S., Mutter, D., Marescaux, J., De Mathelin, M., and Padoy, N. Endonet: a deep architecture for recognition tasks on laparoscopic videos. *IEEE transactions on medical imaging*, 36(1):86–97, 2016.
- Uziel, R., Dinari, O., and Freifeld, O. From vit features to training-free video object segmentation via streaming-data mixture models. In *Advances in Neural Information Processing Systems 36: Annual Conference on Neural Information Processing Systems 2023, NeurIPS 2023, New Orleans, LA, USA, December 10 - 16, 2023*, 2023.
- Van der Maaten, L. and Hinton, G. Visualizing data using t-sne. *Journal of machine learning research*, 9(11), 2008.
- Van Steenkiste, S., Kurach, K., Schmidhuber, J., and Gelly, S. Investigating object compositionality in generative adversarial networks. *Neural Networks*, 130:309–325, 2020.
- Vaswani, A., Shazeer, N., Parmar, N., Uszkoreit, J., Jones, L., Gomez, A. N., Kaiser, L., and Polosukhin, I. Attention is all you need. In *Advances in Neural Information Processing Systems 30: Annual Conference on Neural Information Processing Systems 2017, December 4-9, 2017, Long Beach, CA, USA*, pp. 5998–6008, 2017.
- Vincent, P., Larochelle, H., Lajoie, I., Bengio, Y., Manzagol, P.-A., and Bottou, L. Stacked denoising autoencoders: Learning useful representations in a deep network with a local denoising criterion. *Journal of Machine Learning Research*, 2010.
- Wang, L., Lu, H., Wang, Y., Feng, M., Wang, D., Yin, B., and Ruan, X. Learning to detect salient objects with image-level supervision. In *2017 IEEE Conference on Computer Vision and Pattern Recognition, CVPR 2017, Honolulu, HI, USA, July 21-26, 2017*, pp. 3796–3805, 2017.
- Wang, R., Chen, D., Wu, Z., Chen, Y., Dai, X., Liu, M., Jiang, Y.-G., Zhou, L., and Yuan, L. Bevt: Bert pre-training of video transformers. In *Proceedings of the IEEE/CVF Conference on Computer Vision and Pattern Recognition*, 2022.
- Watters, N., Matthey, L., Burgess, C. P., and Lerchner, A. Spatial broadcast decoder: A simple architecture for learning disentangled representations in vaes. *ArXiv preprint*, abs/1901.07017, 2019.
- Wei, C., Fan, H., Xie, S., Wu, C., Yuille, A. L., and Feichtenhofer, C. Masked feature prediction for self-supervised visual pre-training. In *IEEE/CVF Conference on Computer Vision and Pattern Recognition, CVPR 2022, New Orleans, LA, USA, June 18-24, 2022*, pp. 14648–14658, 2022.
- Weis, M. A., Chitta, K., Sharma, Y., Brendel, W., Bethge, M., Geiger, A., and Ecker, A. S. Unmasking the inductive biases of unsupervised object representations for video sequences. *ArXiv preprint*, abs/2006.07034, 2020.
- Wu, Z., Dvornik, N., Greff, K., Kipf, T., and Garg, A. Slotformer: Unsupervised visual dynamics simulation with object-centric models. In *The Eleventh International Conference on Learning Representations, ICLR 2023, Kigali, Rwanda, May 1-5, 2023*, 2023a.
- Wu, Z., Hu, J., Lu, W., Gilitschenski, I., and Garg, A. Slotdiffusion: Object-centric generative modeling with diffusion models. In *Advances in Neural Information*

Processing Systems 36: Annual Conference on Neural Information Processing Systems 2023, NeurIPS 2023, New Orleans, LA, USA, December 10 - 16, 2023, 2023b.

Xu, J., De Mello, S., Liu, S., Byeon, W., Breuel, T., Kautz, J., and Wang, X. Groupvit: Semantic segmentation emerges from text supervision. In *Proceedings of the IEEE/CVF Conference on Computer Vision and Pattern Recognition*, pp. 18134–18144, 2022.

Xu, J., Lan, C., Xie, W., Chen, X., and Lu, Y. Slot-vlm: Object-event slots for video-language modeling. In *The Thirty-eighth Annual Conference on Neural Information Processing Systems*, 2024.

Xu, N., Yang, L., Fan, Y., Yang, D., Yue, D., Liang, Y., Price, B., Cohen, S., and Huang, T. Youtube-vis: A large-scale video instance segmentation benchmark. In *Proceedings of the IEEE/CVF International Conference on Computer Vision (ICCV)*, pp. 2012–2021, 2019.

Zadaianchuk, A., Seitzer, M., and Martius, G. Object-centric learning for real-world videos by predicting temporal feature similarities. In *Advances in Neural Information Processing Systems 36: Annual Conference on Neural Information Processing Systems 2023, NeurIPS 2023, New Orleans, LA, USA, December 10 - 16, 2023, 2023.*

Zhang, D., Meng, D., Li, C., Jiang, L., Zhao, Q., and Han, J. A self-paced multiple-instance learning framework for co-saliency detection. In *2015 IEEE International Conference on Computer Vision, ICCV 2015, Santiago, Chile, December 7-13, 2015*, pp. 594–602, 2015.

Zhou, T., Wang, S., Zhou, Y., Yao, Y., Li, J., and Shao, L. Motion-attentive transition for zero-shot video object segmentation. In *The Thirty-Fourth AAAI Conference on Artificial Intelligence, AAAI 2020, The Thirty-Second Innovative Applications of Artificial Intelligence Conference, IAAI 2020, The Tenth AAAI Symposium on Educational Advances in Artificial Intelligence, EAAI 2020, New York, NY, USA, February 7-12, 2020*, pp. 13066–13073, 2020.

Zia, A., Bhattacharyya, K., Liu, X., Berniker, M., Wang, Z., Nespolo, R., Kondo, S., Kasai, S., Hirasawa, K., Liu, B., et al. Surgical tool classification and localization: results and methods from the miccai 2022 surgtoolloc challenge. *ArXiv preprint*, abs/2305.07152, 2023.

Supplementary Material

A. Extended Implementation Details

Section 4.4 presents the main experimental setup and model overview. Here, we provide additional implementation details covering network components, hyperparameters, and optimization settings across all experiments.

Network Architecture and Training Hyperparameters

Our implementation is based on the Object Centric Learning framework with PyTorch. We set the same fixed learning rate (1.0×10^{-4}) weight decay (1.0×10^{-5}) and gradient clipping (0.05) for all modules for all the ablation studies and other parameter tuning (e.g. tuning of temperature and slot number parameter) experiments.

Feature Encoder We use a self-supervised Vision Transformer (ViT) as the feature encoder, following the work on object centric learning in real-world images or videos (Seitzer et al., 2023; Zadaianchuk et al., 2023). Specifically, we employ a DINO ViT backbone (vit_base_patch16_224_dino) (Caron et al., 2021) that encodes 224×224 pixel resized images into patch embeddings. Patches are extracted with size $P = 16$ pixels, resulting in $N = 196$ spatial feature locations per frame.

Slot Attention Module Slot Attention is applied independently per frame to decompose spatial features into K latent object slots. Encoder features are linearly projected to the slot dimension and normalized. Slot Attention is iterated for n_{iters} steps per frame using scaled dot-product attention, GRU-based slot updates, and an MLP with residual connections. First frame slots are randomly initialized for the first frame using a Gaussian distribution and propagated temporally for subsequent frames. Configuration details are summarized in Table S1.

Table S1. Slot Attention Module Configuration

Parameter	Value
Number of slots (K)	7
Slot dimension (d_{slot})	64
Slot attention iterations (n_{iters})	3 for first frame, 2 per other frames
Initialization strategy	Random Gaussian (first frame)
Encoder output dim (D_{feat})	768
MLP hidden dim	[1024]

TST module TST module operates on slot embeddings of shape $[B, T, K, d_{\text{slot}}]$. The TST consists of three transformer encoder layers with 8 attention heads and feed-forward dimension $4 \times d_{\text{slot}}$. Learnable temporal positional embeddings are added to slot representations. During training, random temporal masking with ratio $\gamma = 0.20$ is applied for regularization. Full settings are listed in Table S2.

Table S2. Temporal Slot Transformer (TST) Module Configuration

Parameter	Value
Number of transformer layers	3
Attention heads per layer (n_{heads})	8
Feed-forward hidden dimension	$4 \times d_{\text{slot}} = 256$
Masking ratio (γ)	0.20
Temporal positional embeddings	Learnable, shape $[1, T, 1, d_{\text{slot}}]$
Activation function	GELU

Slot Decoder We consider an MLP decoder and a Slot-Mixer decoder. The MLP decoder independently maps each slot to spatial predictions using slot broadcasting and fully connected layers with additive positional embeddings. The Slot-Mixer decoder incorporates a transformer-based allocator (3 blocks, 4 attention heads) to jointly reason over slots prior to MLP-based rendering. Both decoders employ layer normalization for training stability. Unless otherwise stated, all parameter tuning and ablation studies are conducted using the MLP decoder. Detailed configurations are provided in Table S3.

Table S3. Slot Decoder Variants Configuration

Decoder Type	Component	Configuration
MLP	Hidden layers	[512, 512, 512, 512]
	Additive position embedding	[196, 64]
	Normalization	Layer normalization
Slot-Mixer	Allocator	Transformer, 3 blocks, 4 heads
	MLP renderer	[1024, 1024], output dim 1024
	Additive position embedding	[196, 64]
	Normalization	Layer normalization

B. Illustration of using TST module for next slot initialization

In Section 4.8 of the main text, we present the results of adapting pre-trained slot-BERT for longer sequence prediction. In addition to using a traditional approach for slot initialization, where the previously predicted slot is fed into the next slot encoder as an initializer, we also demonstrate an alternative option of using the same TST module as a slot initializer, as shown in Figure S1. In this new design, we take the previous slot buffer \dots, s_{t-1}, s_t and append an empty slot (zero vectors) to the latest position. The only modification to the TST module is to switch it from random masking to fixing the mask at the last location, enabling the TST module to predict the missing empty slot by reasoning over the historical slots. Finally, the next slot encoder takes the predicted slot from the TST module, s_{t+1}^i , as the initialization to update slot s_{t+1} . In our experiment, instead of creating a new TST module for the initializer or freezing the pre-trained TST for postprocessing, we allow the initializer and slot decoder to share weights from the same TST

module and enable end-to-end training with the new slot initializer.

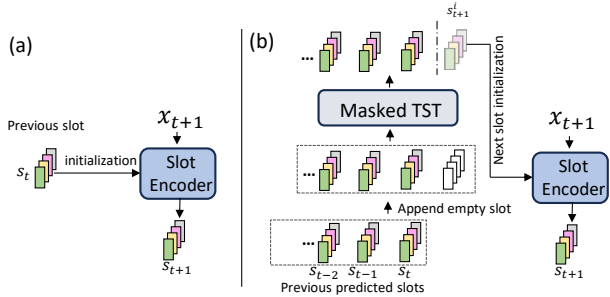


Figure S1. Schematic illustration of next-slot initialization using TST. (a) Conventional slot initialization techniques, such as those used in RNN-based video slot attention algorithms. (b) Integration of same TST module as a slot initializer by appending an empty slot and masking the last embedding position. The predicted missing slot is then used to initialize the next slot prediction.

C. Visualization of channel-wise object-centric attention overlay

We provide extended visualizations of the slot attention maps across independent channels (Figure S2). Following the presentation style of Figure 6, to indicate correspondence, the slot index number is overlaid in white on each colored mask of the first frame. In this example, Slot-BERT is trained with seven slots for surgical videos, where these slots are allocated to attend to different instruments and tissue regions.

D. Visualization of latent slot embedding projection

To investigate the distinctiveness and relationships among slot vectors, we first visualize the latent slot embeddings learned by Slot-BERT using t-SNE (Van der Maaten & Hinton, 2008). As shown in Figure S3, slot vectors corresponding to different instruments within a video tend to cluster closer to each other, while remaining distinct from the clusters of tissue-related slot vectors. This behavior highlights the disentangled and interpretable nature of the slot representations learned by our approach.

To further validate this observation, we applied Principal Component Analysis (PCA), a linear projection method that preserves the relative distances between data points in the latent space. The PCA mapping also reveals clear separation between regions corresponding to instrument slots and tissue slots, while maintaining the internal distinctiveness of each category. These results indicate that the slot embeddings learned by Slot-BERT are both robust and explainable, effectively capturing the compositional structure of objects

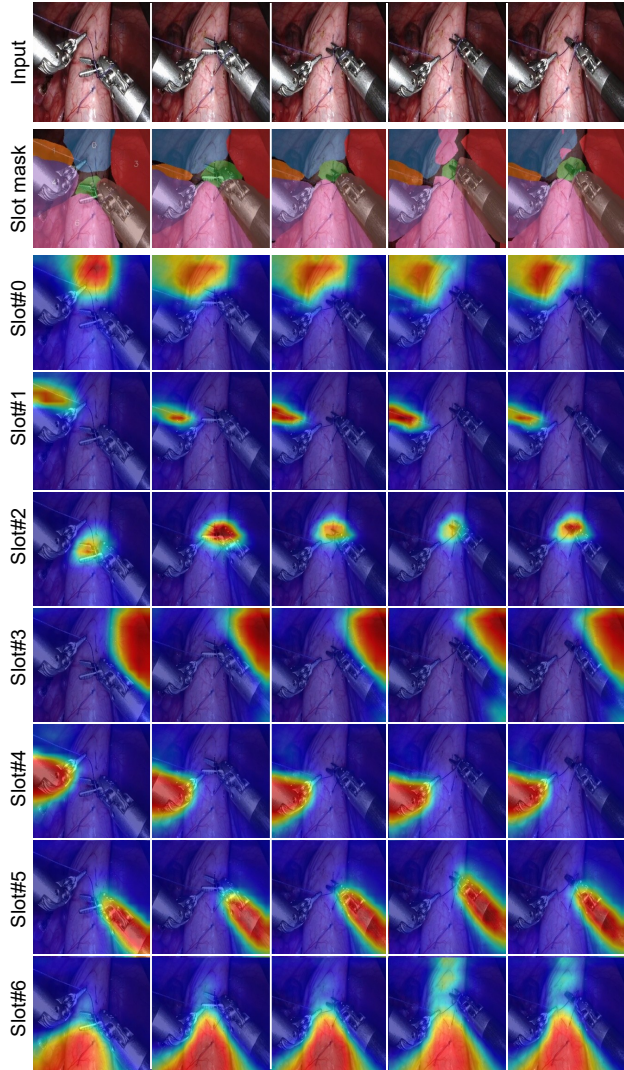


Figure S2. Visualization of multi-channel object-centric slot attention. We present both the binarized slot masks and the corresponding attention heatmaps for each slot. To indicate correspondence, the slot index is also overlaid in white on each colored mask of first frame.

in video data.

E. Results of different slot numbers with additional metrics

In section 4.13 we present the results of our method using different slot numbers. And demonstrated that with slot number 7 it shows optimal localization accuracy when either MLP or slot-Mixer decoder is adopted for Slot-BERT. Here detailed quantitative results on additional metrics is revealed in table S4. As shown in Table S4, specifically, with 7 slots and an MLP decoder, the CorLoc metric reaches its peak at 70.7 ± 0.8 in the training domain, and mBHD

Table S4. This table presents the performance of our method with varying slot numbers (K) using both MLP and Slot-Mixer decoders across multiple evaluation metrics. The metrics include mBO-V, mBO-F, mBHD (boundary localization), FG-ARI, and CorLoc (spatial localization) in both the training and zero-shot domains. Notably, using an MLP decoder with 7 slots yields the highest CorLoc and mBHD scores in the training domain, while a Mixer decoder with 9 slots shows higher mBO-F and mBO-V results in both domains.

Decoder	K	Training Domain				Zero-Shot Domain					
		mBO-V (%)	mBO-F (%)	mBHD (\downarrow)	FG-ARI (%)	CorLoc (%)	mBO-V (%)	mBO-F (%)	mBHD (\downarrow)	FG-ARI (%)	CorLoc (%)
MLP	3	37.8 \pm 0.3	40.5 \pm 0.2	101.46 \pm 0.93	42.3 \pm 0.3	52.1 \pm 0.4	33.4 \pm 0.2	35.7 \pm 0.1	100.59 \pm 0.33	38.8 \pm 0.1	49.2 \pm 0.5
	5	45.6 \pm 0.4	48.9 \pm 0.5	53.25 \pm 2.21	53.1 \pm 0.6	66.2 \pm 0.8	40.8 \pm 0.1	44.2 \pm 0.1	61.10 \pm 0.35	49.7 \pm 0.1	61.9 \pm 0.5
	7	48.9 \pm 0.2	52.8 \pm 0.2	43.40 \pm 0.53	58.2 \pm 0.3	70.7 \pm 0.8	44.0 \pm 0.2	48.4 \pm 0.1	49.26 \pm 0.93	55.2 \pm 0.3	62.8 \pm 0.2
	9	49.1 \pm 0.5	54.3 \pm 0.1	41.81 \pm 0.94	60.1 \pm 0.2	69.0 \pm 0.5	44.4 \pm 0.1	49.4 \pm 0.2	49.43 \pm 0.18	56.9 \pm 0.3	59.4 \pm 0.5
	11	49.2 \pm 0.3	53.6 \pm 0.1	44.47 \pm 0.19	60.0 \pm 0.2	63.7 \pm 0.8	44.6 \pm 0.4	48.9 \pm 0.1	50.82 \pm 0.43	57.1 \pm 0.2	51.2 \pm 0.5
Mixer	3	33.9 \pm 0.4	36.3 \pm 0.3	114.97 \pm 1.23	36.2 \pm 0.4	43.9 \pm 0.8	30.0 \pm 0.1	32.5 \pm 0.1	110.21 \pm 0.36	34.1 \pm 0.1	39.6 \pm 0.1
	5	45.2 \pm 0.0	48.9 \pm 0.1	59.85 \pm 0.57	52.6 \pm 0.2	62.3 \pm 1.0	40.2 \pm 0.2	43.6 \pm 0.2	63.13 \pm 0.60	49.0 \pm 0.1	59.7 \pm 0.2
	7	49.0 \pm 0.4	53.2 \pm 0.2	46.99 \pm 1.01	58.2 \pm 0.2	67.4 \pm 0.9	43.2 \pm 0.2	47.5 \pm 0.2	51.95 \pm 0.50	54.3 \pm 0.1	61.9 \pm 0.3
	9	49.3 \pm 0.9	53.7 \pm 0.7	46.41 \pm 0.98	59.7 \pm 0.7	61.9 \pm 1.0	44.0 \pm 0.3	49.1 \pm 0.1	51.03 \pm 0.18	56.6 \pm 0.1	57.5 \pm 0.5
	11	47.7 \pm 0.6	52.5 \pm 0.2	49.73 \pm 0.62	59.1 \pm 0.1	55.6 \pm 0.6	43.7 \pm 0.3	48.8 \pm 0.2	53.14 \pm 0.65	57.1 \pm 0.3	48.7 \pm 0.5

Table S5. Transfer learning vs from scratch learning with Endovis and Thoracic dataset. The transfer learning uses models pre-trained on MICCAI dataset as initialization, and fine-tune them on the target domain data for 80 epoches. From scratch learning directly train the model on target domain for 2000 epoches.

Dataset	Method	Transfer learning				From scratch			
		mBO-V(%)	mBO-F(%)	mBHD (\downarrow)	FG-ARI(%)	mBO-V(%)	mBO-F(%)	mBHD (\downarrow)	FG-ARI(%)
Endovis	DINO-Saur(Seitzer et al., 2023)	38.8	44.1	52.4	51.3	25.6	26.1	122.5	29.4
	SAVi(Kipf et al., 2022)	30.3	34.1	77.8	39.3	34.4	38.5	110.9	42.9
	STEVE(Singh et al., 2022)	26.4	30.3	147.2	34.5	31.5	34.1	97.9	38.6
	Slot-Diffusion(Wu et al., 2023b)	36.2	38.5	66.7	43.3	42.3	46.0	56.9	53.2
	Video-Saur(Zadaianchuk et al., 2023)	46.9	51.2	50.8	57.8	25.7	25.8	135.0	39.4
	Ours	48.8	52.3	41.7	59.2	45.1	46.0	70.1	51.6
Thoracic	DINO-Saur(Seitzer et al., 2023)	31.1	39.3	86.0	32.5	27.1	30.7	104.8	23.9
	SAVi(Kipf et al., 2022)	25.6	28.7	106.5	22.5	26.5	30.7	119.8	23.1
	STEVE(Singh et al., 2022)	23.8	30.0	131.9	22.3	28.9	33.0	135.4	26.5
	Slot-Diffusion(Wu et al., 2023b)	29.9	37.8	104.3	28.8	31.1	39.9	84.6	31.4
	Video-Saur(Zadaianchuk et al., 2023)	38.9	52.1	65.7	41.9	21.9	15.7	139.5	11.9
	Ours	39.9	52.1	65.2	41.7	34.0	40.5	92.4	33.8

achieves its value of 43.40 ± 0.53 , reflecting accurate boundary localization. Similarly, with the Slot-Mixer decoder and 7 slots, the CorLoc metric achieves its highest value of 67.4 ± 0.9 , demonstrating robust spatial localization.

When extending the analysis to evaluate segmentation overlap on the training and zero-shot domains, using 9 slots emerges as a strong performer. With the MLP decoder, 9 slots achieve the highest mBO-F at 54.3 ± 0.1 in the training domain and 49.4 ± 0.2 in the zero-shot domain. Moreover, the Slot-Mixer decoder with 9 slots delivers the best mBO-V scores of 49.3 ± 0.9 for the training and zero-shot domains, respectively, signifying enhanced temporal coherence in video object segmentation.

These results underscore the nuanced trade-offs across different slot numbers and decoder configurations. While slot number 7 provides strong spatial localization, slot number 9 excels in overlap accuracy and temporal consistency, making it a versatile choice depending on the task emphasis.

F. Additional results on transfer learning on Endovis and Thoracic data

We fine-tuned the MICCAI pre-trained model on the Endovis and Thoracic datasets for 80 epochs as an extension of the transfer learning experiment. Additionally, we trained all

models from scratch on the Endovis and Thoracic datasets for 2000 epochs, to compare their performance with transfer learning. To effectively utilize the small Endovis and Thoracic datasets for fine-tuning, following previous unsupervised segmentation approaches (Zhang et al., 2015; Wang et al., 2017), we allowed the model access to the full Endovis and Thoracic videos. Our goal was to evaluate whether the models could generate accurate pseudo-masks under the condition of no ground truth supervision signals.

As presented in Table S5, after fine-tuning on these two domain-specific datasets (Endovis and Thoracic) using only self-supervised objectives such as reconstruction and contrastive learning, without relying on any labels, our method further improves performance. Remarkably, the fine-tuned results surpass those of models trained from scratch. For example, in Endovis, our fine-tuned model achieves an FG-ARI of 59.2%, which is higher than the scratch-trained model’s FG-ARI of 51.6%. Similarly, on the Thoracic dataset, our method achieves notable gains in mBO-V and FG-ARI after fine-tuning, demonstrating the effectiveness of leveraging knowledge obtained from unsupervised pretraining on MICCAI data. It is worth noting that for some methods (e.g., Slot Diffusion and STEVE), transfer learning did not outperform training from scratch. This could possibly be because these methods tend to overfit on small datasets

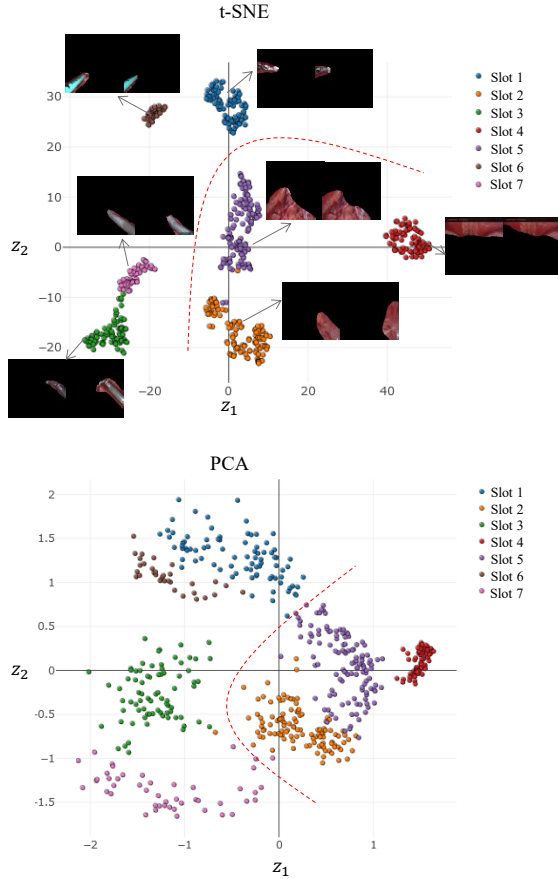


Figure S3. Visualization of latent slot embeddings using t-SNE and PCA. Slot embeddings were extracted from a concatenated long video consisting of 100 frames (7 slots per frame) from the MICCAI challenge dataset. The scatter plots illustrate the clustering of slot vectors in the latent space. Example images decoded from corresponding slot masks are displayed alongside their projected points, demonstrating the separation of instrument slots and tissue slots into distinct and meaningful clusters.

rather than generalize and effectively leverage knowledge across domains.

G. Additional ablation study on slot masks

We also examined the impact of slot-specific masking by directly inputting video slots into the TST module without applying slot masks and replacing the masked transformer with a standard transformer (referred to as w/o slot masks). This led to a slight performance degradation. As shown in Table S6, on the MICCAI dataset (long sequences), the mBO-V score was 45.9% compared to 46.9% for the full model. This suggests that slot masks do contribute to robust representation learning by focusing on relevant feature regions.

In addition, we replaced slot-specific masking with feature-level masking. A masked autoencoding strategy was applied, where random feature patches were masked during training (denoted as maskout feature). This configuration showed further degradation in performance compared to the full model. For example, on the Thoracic dataset, the mBO-V score was 32.9%, significantly lower than the 37.7% achieved by the full model. This indicates that random feature masking is less effective than the structured masking strategy employed by the slot-BERT module.

H. Additional Results on Non-Surgical Data

We additionally evaluate Slot-BERT on non-surgical datasets, including the natural real-world dataset YT-VIS (Xu et al., 2019) and the synthetic dataset MOVi-E (Greff et al., 2022). Following prior work (Wu et al., 2023b; Zadaianchuk et al., 2023), we use 7 slots for training on YT-VIS and 15 slots for MOVi-E. For evaluation, we sample 6 frames on YT-VIS and 24 frames on MOVi-E, consistent with the setup in Video-Saur (Zadaianchuk et al., 2023).

As shown in Table S7, on the real-world YT-VIS dataset our method outperforms the second-best Video-Saur by over +6% mBO-V. On the synthetic MOVi-E dataset, Slot-BERT achieves comparable FG-ARI performance to Video-Saur. We note that MOVi-E provides less challenging conditions for object discovery due to its fixed camera viewpoint and relatively simple backgrounds which likely reduces the performance gap between methods.

I. Additional qualitative results

I.1. Comparison on using MLP and slot-Mixer decoder

In Section 4.11, we present the results of using the alternative Slot-Mixer decoder instead of the MLP decoder (as explained in Section 3.5) to reconstruct target features, exploring various setup variations. Detailed qualitative comparisons between different decoders are provided here. Figure S4 illustrates segmentation masks produced by Slot-BERT with both MLP and Slot-Mixer decoders, tested on sequences of 30 frames at 1 FPS from the MICCAI dataset. The model was trained using 7 slots.

Both MLP and Slot-Mixer decoders demonstrate unique strengths. With the MLP decoder, the segmentation masks tend to cover objects more comprehensively and accurately locate them. On the other hand, the Slot-Mixer decoder exhibits superior temporal consistency, since its within-frame attention at decoding provides synergistic benefits when combined with the temporal attention (TST), further stabilizing segmentation across video frames. For instance, in the first and third rows of Figure S4, the instrument un-

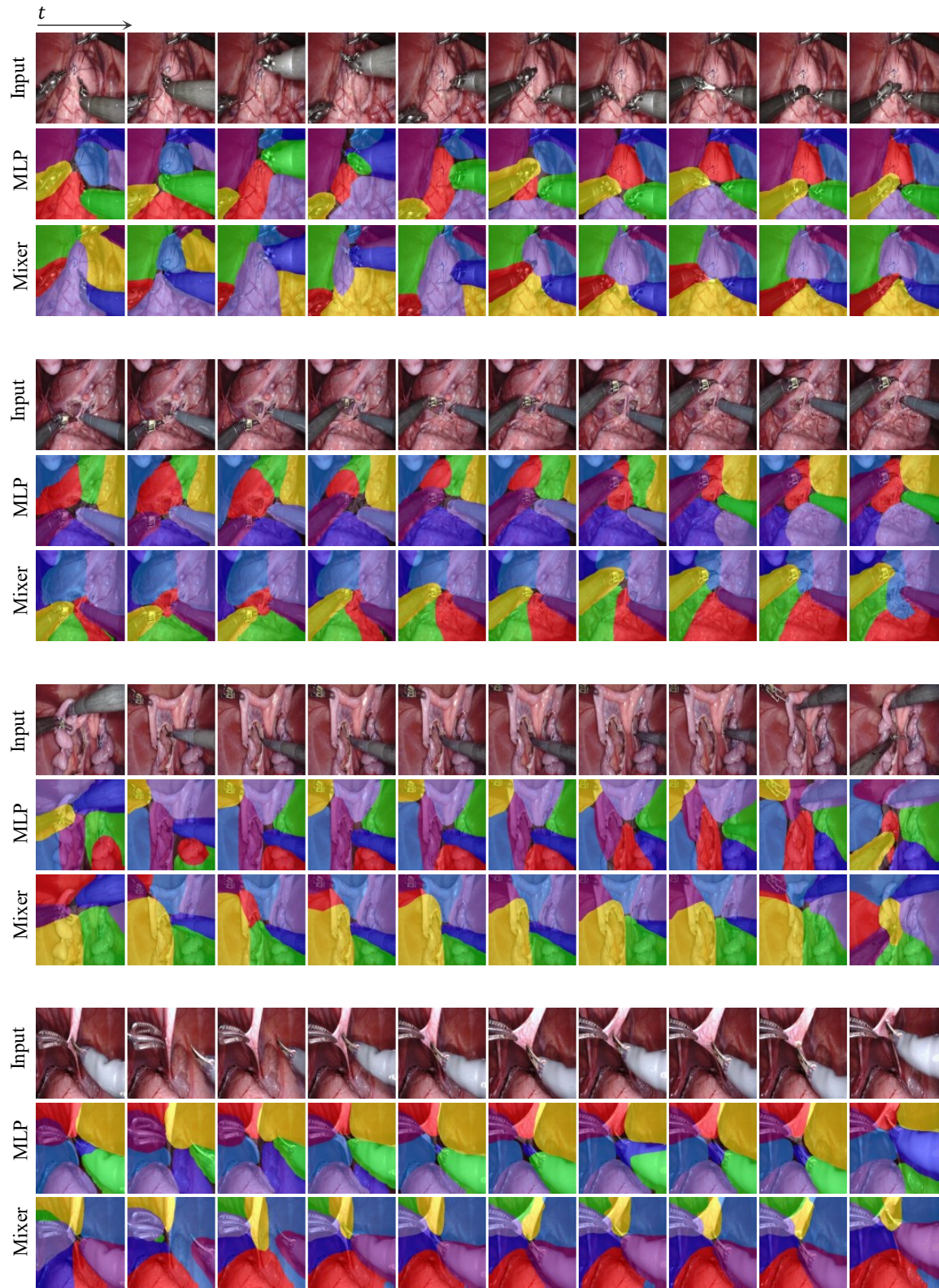


Figure S4. Qualitative results of Slot-BERT with MLP and Slot-Mixerdecoder tested on longer sequences of 30 frames (1 FPS) from the MICCAI dataset. The model was trained with 7 slots. Each output sequence has been downsampled by a factor of 3, and 10 samples are displayed.

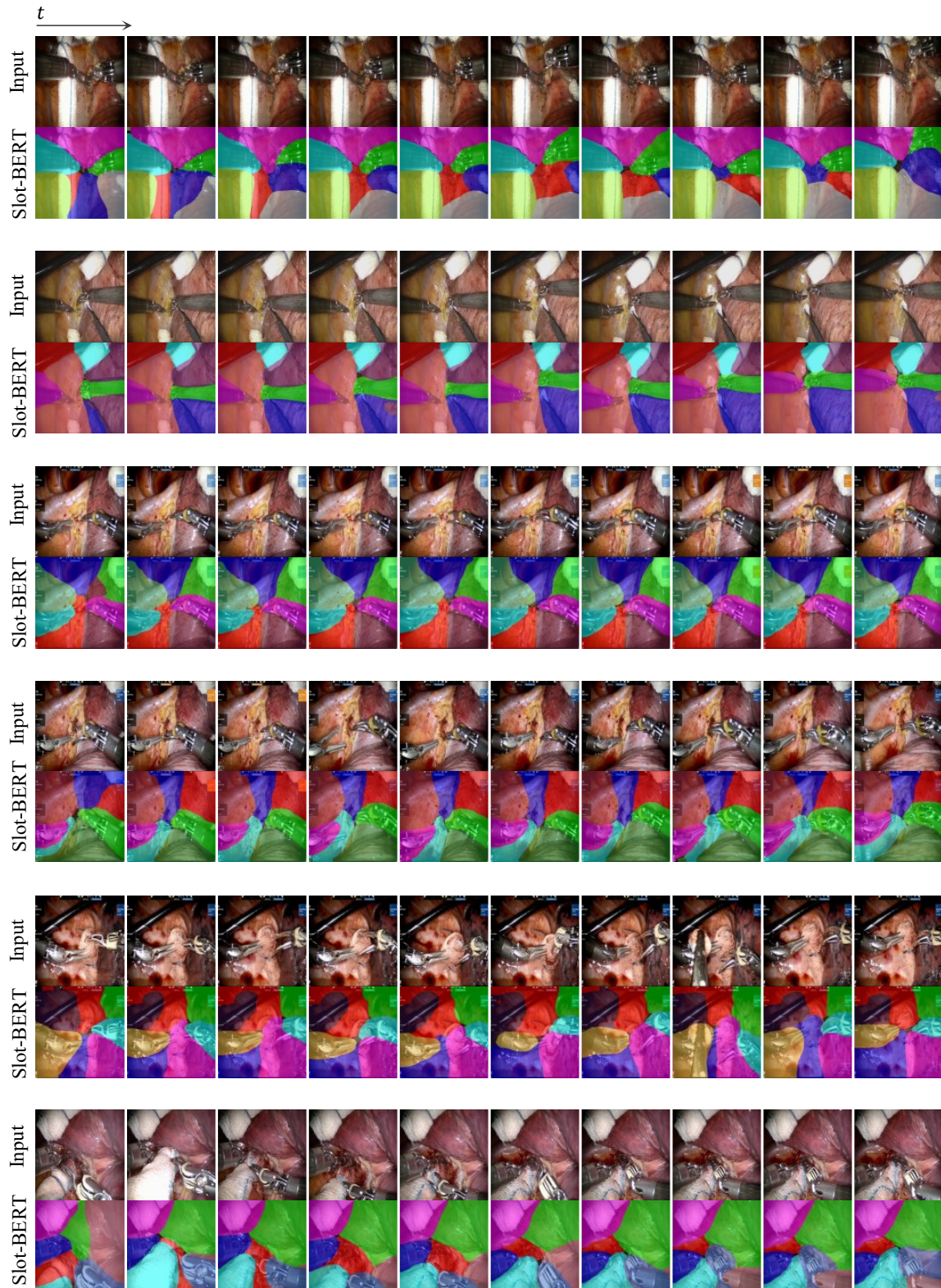


Figure S5. Zero-shot transfer of Slot-BERT with Mixer decoder to thoracic robotic surgery videos after training on MICCAI abdominal data. The test sequence consists of 30 frames, downsampled to 10 frames for presentation. Notably, in some images, a slot successfully attends to gauze, an unseen object in the MICCAI dataset.

Table S6. Additional ablation on the slot masks. The performance is tested under the training domain (MICCAI) and zero-shot transfer domain (EndoVis and Thoracic)

Method	Same domain (MICCAI)				Zero shot transfer			
	5 frames		11 frames		Endovis		Thoracic	
	mBO-V (%)	FG-ARI (%)	mBO-V (%)	FG-ARI (%)	mBO-V (%)	FG-ARI (%)	mBO-V (%)	FG-ARI (%)
maskout feature	45.8 ± 0.5	55.0 ± 0.5	42.2 ± 0.6	53.6 ± 0.7	41.0 ± 0.5	51.7 ± 0.3	32.9 ± 0.2	36.6 ± 0.1
w/o slot masks	48.6 ± 0.3	57.6 ± 0.5	45.9 ± 0.9	57.1 ± 0.4	43.0 ± 0.3	53.9 ± 0.2	35.0 ± 0.1	38.7 ± 0.1
our full	48.9 ± 0.2	58.2 ± 0.3	46.9 ± 0.0	57.3 ± 0.3	44.0 ± 0.2	55.2 ± 0.3	37.7 ± 0.2	40.5 ± 0.1

Table S7. Additional results on non-surgical datasets YT-VIS (Xu et al., 2019) and MOVi-E (Greff et al., 2022). Results are reported in terms of mBO-V and FG-ARI. Best results are highlighted in bold.

Method	YT-VIS		MOVi-E	
	mBO-V	FG-ARI	mBO-V	FG-ARI
SAVi (Kipf et al., 2022)	13.6	22.2	23.5	46.7
STEVE (Singh et al., 2022)	26.5	36.1	27.9	56.0
Slot-Diffusion (Wu et al., 2023b)	28.9	14.7	30.2	60.0
Video-Saur (Zadaianchuk et al., 2023)	29.1	39.5	35.6	73.9
Slot-BERT (ours)	35.3	41.1	35.4	74.3

dergoes significant motion (e.g., moving across the image within a few frames). While the MLP decoder loses track of the object during such maneuvers, the Slot-Mixer decoder successfully maintains object tracking. This is evident in the image sequence, where the Slot-Mixer preserves the correct mask order despite the large motion, showcasing its robustness in maintaining temporal coherence.

I.2. Zero-shot Segmentation of longer video sequence

As discussed in Section 4.7 of the main text, the model trained on MICCAI abdominal data demonstrates strong performance on thoracic data, which involves similar instruments but different tissue backgrounds. Figure S5 presents qualitative segmentation results for the zero-shot transfer of Slot-BERT with the Mixer decoder applied to thoracic robotic surgery videos.

Despite the differences in tissue backgrounds, the model effectively segments and tracks instruments. Notably, a slot successfully attends to gauze, an object not present in the MICCAI dataset, as seen in the first, second, and sixth rows. For instruments that are common between the MICCAI abdominal surgery data and the thoracic videos, such as needle drivers, the model achieves superior segmentation results, showcasing its ability to generalize across different surgical contexts.